

Phase-field study of the electric current induced void evolution and grain-boundary grooving

A Thesis
Submitted for the fulfillment of Degree of
Master of Engineering
in Materials Engineering

By
Supriyo Chakraborty
Supervisor
Dr. Abhik Choudhury



Department of Materials Engineering
Indian Institute of Science
Bangalore - 560012 , India
June 2016

**Dedicated to
My Mother**

Synopsis

Electric current can induce mass transport in a conductor. But to observe a significant mass transport very high current density is required. This situation is encountered in the thin film interconnects inside the electronic chips and devices. Current density of $10^6 A/cm^2$ can easily be seen in the thin film interconnects. First of all, this much of current density gives rise to joule heating in the circuit, due to which mass transport becomes easier at elevated temperature. Electrons flowing inside the conductor can collide with the diffusing ions and transfer its momentum to the ions. The magnitude of the momentum transfer depends on the number of electrons colliding with the ions. So, with the increase in current density chances of colliding with an ion increase. The ion experiences a force on itself in the direction of cathode to anode. When this force is sufficiently high ions start to migrate from cathode to anode region and leave a region of void on the cathode side. This phenomenon is known as electromigration.

The real situation is more complex due to the presence of temperature gradient, stress field inside the interconnects. These forces also affect the void evolution inside the interconnects. Thin film interconnects have a large area of free surface which provides an easy way of diffusion. Also, thin film interconnects are polycrystalline in nature which provides a pathway for mass transport through the grain boundaries. So, to understand the interconnect failure mechanisms we need to consider all of these complexities. In our study we are going to use a phase field model to describe this physical phenomenon and study the effect of different forces on the mass transport in the interconnects.

A novel phase field model has been developed to understand the void migration and growth in interconnects due to electromigration. Using this model we have successfully simulated the characteristics of void morphologies. It is observed that for low current densities the growing voids retain their shape, while for higher current densities, the

voids get elongated. The calculated velocity of void migration and their volume have been found to be linearly varying with the applied potential difference, which agrees well with the theoretical predictions. Subsequently, we have investigated the influence of anisotropy in surface energy and surface diffusivity on the void morphologies.

Thereafter, we have extended our model to incorporate multi-phase system to study the more realistic situation of polycrystalline interconnects. Firstly, we have simulated grain-boundary grooving at free surface and grain boundary migration under electromigration conditions in 2D, for a system of two grains. Here, we have also compared our results with the analytical theories available for grain-boundary grooving without electromigration. In the presence of electric current we have found unsymmetrical groove profile across the groove root. The profile takes a ridge like shape on the cathode side and a hillock is formed on the anode side. Next, we have done 3D simulation to observe the effect of multigrain. We have found pit formation around the grain boundary triple points.

Lastly, we have investigated the effect of temperature gradient on mass transport and coupled it with the electromigration. Here, we have introduced a random polycrystalline solid phase to study the effect of grain boundaries. we have simulated the higher rate of mass transport from the cathode side and an anomalous back flow of atoms from anode side. The interplay between these two driving forces determine the nature of void evolution inside the interconnect. We have also studied the effect of grain size on the mass flow. The microstructure having bigger grains has shown slower mass transport than the microstructure with smaller grain size.

Contents

List of Figures	vi
1 Introduction	1
2 Literature Review	3
2.1 Electromigration	3
2.2 Grain boundary grooving	4
2.3 Thermomigration	5
2.4 Basic equations	6
2.5 Phase field model	7
2.5.1 Phase field model of electromigration	7
2.5.2 Phase field model of thermomigration	8
3 Model Formulation	9
3.1 Isotropic formulation	9
3.2 Implementing anisotropy	12
3.2.1 Anisotropic diffusivity	12
3.2.2 Anisotropic surface energy	13
3.3 Multi-phase field model	15
4 Void Evolution in Presence of Electric Current	20
4.1 Defining parameters	20
4.2 1D results	21
4.3 2D results	21
4.3.1 Isotropic case	21
4.3.2 Anisotropic surface energy	26
4.3.3 Diffusivity anisotropy	27

5 Grain Boundary Grooving and Effect of Electric Current	29
5.1 2D simulation of grain boundary grooving	29
5.1.1 Model system	29
5.1.2 Comparison with Mullins theory	30
5.2 3D simulation of grain boundary grooving	34
5.2.1 Model system	34
5.2.2 Pit formation at grain boundary vertices	35
5.3 Effect of electric current on grain boundary grooving	37
5.3.1 Grain boundary migration under electric current	38
5.3.2 2D simulation results	39
5.3.3 3D simulation results	45
6 Mass Transport Under Electric Current and Temperature Gradient	47
6.1 Mass transport through a grain boundary	48
6.1.1 Effect of electric current	48
6.1.2 Effect of temperature gradient	49
6.1.3 Combined effect of electric current and temperature gradient . .	50
6.2 Mass transport in a polycrystalline solid	52
6.2.1 Simulation results for cathode side	53
6.2.2 Simulation results for anode side	54
6.2.3 Effect of grain size	56
7 Summary and Conclusion	58
8 Future Works	62
Appendix A Numerical Methods	63
A.1 Thomas Algorithm	63
A.2 Red-black Gauss-Seidel method	64
A.3 Discretization Scheme	65
A.3.1 Discretization of isotropic model	65
A.3.2 Discretization of anisotropic model	67
A.4 Voronoi tessellation for polycrystalline microstructure	69
Bibliography	71

List of Figures

2.1	Forces on an ion inside a conductor.	3
2.2	Grain boundary groove profile due to curvature driven mass transport.	4
2.3	Grain boundary groove profile in the presence of electric current flowing from left to right[4].	5
2.4	Current crowding at the corners[7].	5
2.5	Typical temperature profile due the current crowding.	6
4.1	(a) ϕ profile where $\phi = 0$ is void and $\phi = 1$ is solid;(b) electric potential profile where left terminal is cathode(-ve) and right terminal is anode(+ve).	21
4.2	Initial condition for all the cases.	22
4.3	simulation results for $\chi = 1.225$	22
4.4	simulation results for $\chi = 2.45$	23
4.5	simulation results for $\chi = 4.9$	23
4.6	(a) simulation results for void volume increase with time for different χ values, (b) void shape change with time for different χ	25
4.7	Front velocity of void vs. χ	25
4.8	simulation results with anisotropic surface energy for $\chi = 0.98$	26
4.9	simulation results with anisotropic surface energy for $\chi = 1.96$	26
4.10	simulation results with anisotropic surface energy for $\chi = 4.9$	27
4.11	Anisotropic diffusivity strength $\delta = 0.35$	28
4.12	Anisotropic diffusivity strength $\delta = 0.5$	28
5.1	(a) Initial system, (b) after grooving.	29
5.2	Groove profile for $\frac{\gamma_{gb}}{\gamma_s} = 1.0$ case for different timesteps.	31
5.3	Groove profile for two different $\frac{\gamma_{gb}}{\gamma_s}$ ratio for same timestep.	31
5.4	Measuring groove angle by fitting two polynomials for $\frac{\gamma_{gb}}{\gamma_s} = 1.0$ case. .	32

5.5 Comparison of the phase field model($\frac{\gamma_{gb}}{\gamma_s} = 1.0$) with Mullins analytical solution.	33
5.6 Groove depth and hillock height vs. time for $\frac{\gamma_{gb}}{\gamma_s} = 1.0$	33
5.7 Separation between two hillocks vs. time for $\frac{\gamma_{gb}}{\gamma_s} = 1.0$	34
5.8 Surface Plot(X-Z plane) (a) initial system, (b) after smoothing steps. .	35
5.9 Solid-vapour interface plot (x-z plane) for two different timesteps. . . .	36
5.10 (a) Pit depth follows a $t^{1/4}$ time dependence, (b) d_p/d_g ratio ≈ 2	37
5.11 SEM images showing grain boundary hillocks and whisker around grain boundary holes[19], the arrow shows the direction of electron flow. . . .	38
5.12 Schematic showing the grain boundary migration due to distorted groove root.	39
5.13 (a) Initial system (b) after applying electric current.	39
5.14 Evolution of grain boundary groove in the isotropic case for a given voltage difference = 1.5.	40
5.15 Comparison of groove profiles for different potential differences for the same timestep, where $\gamma_{gb}/\gamma_s = 1.0$ for all the cases.	41
5.16 Comparison of groove depth to anode hillock height ratio for different electric potential differences, where $\gamma_{gb}/\gamma_s = 1.0$ for all the cases. . . .	41
5.17 Figure showing the interfaces at different time, blue and green line representing solid-liquid interfaces and red line representing the grain boundary between two solid phases. $\gamma_{gb}/\gamma_s = 1.0$ and applied potential difference is 2.0.	42
5.18 Comparison of the groove root displacement for different potential differences and fitting to $t^{1/4}$ curves; $\gamma_{gb}/\gamma_s = 1.0$ for both the cases. . . .	43
5.19 Comparison of groove profile for two different γ_{gb}/γ_s ratio under the same potential difference = 2.0.	44
5.20 Comparison of groove profile for two different γ_{gb}/γ_s ratio under the same potential difference = 2.0.	44
5.21 Surface plot (x-z plane) for two different time for an applied potential difference of 1.0: observation of (i) anode side hillock formation, (ii) ridge formation near grain boundary groove, (iii) pit formation at the grain boundary vertices and (iv) grain boundary migration towards cathode.	45

5.22 Comparison of pit depth for two different condition.	46
6.1 SEM images of thin film after electromigration test (a) forward mass transport on cathode side, (b) anomalous backward mass transport on anode side; red arrows show the initial positions for cathode and anode[10].	48
6.2 Mass transport through a grain boundary parallel to the applied electric current.	49
6.3 Applied temperature profile along the x-axis.	50
6.4 Mass transport under the temperature gradient.	50
6.5 Schematics to understand the mass transport processes.	51
6.6 Mass transport under different combinations of electric potential gradient and temperature gradient for time = 3840000.	52
6.7 Initial system consisting a void phase (blue) and a polycrystalline solid phase.	52
6.8 Applied temperature profile.	53
6.9 Void phase growth inside the solid phase due to temperature gradient. .	53
6.10 Composition profile due to temperature gradient at time = 576000, red dots showing hillocks.	54
6.11 Void phase growth inside the solid phase due to coupled electric current and temperature gradient, electric potential difference = 0.5.	54
6.12 Void phase growth inside the solid phase due to coupled electric current and temperature gradient, electric potential difference = 1.0.	54
6.13 Applied temperature profile.	55
6.14 Void phase growth inside the solid phase in the presence of temperature gradient.	55
6.15 Composition profile due to temperature gradient at time = 576000, red dots showing hillocks.	55
6.16 Void phase growth inside the solid phase due to coupled electric current and temperature gradient, electric potential difference = 0.1.	56
6.17 No growth of void phase is observed, electric potential difference = 0.5.	56
6.18 Comparison between the two solid phase grain structure.	57
6.19 Comparative study of the effect of grain size on void growth, electric potential difference = 0.5.	57
A.1 Discretization of the domain for calculating $\nabla^2\phi$	65

A.2	Discretization of Laplace equation.	66
A.3	Discretization of ϕ_x for $\frac{\partial}{\partial \phi_x} (a_c \nabla \phi)^2$	67
A.4	Discretization of ϕ_y for $\frac{\partial}{\partial \phi_x} (a_c \nabla \phi)^2$	67
A.5	Discretization of ϕ_x for $\frac{\partial}{\partial \phi_y} (a_c \nabla \phi)^2$	68
A.6	Discretization of ϕ_y for $\frac{\partial}{\partial \phi_y} (a_c \nabla \phi)^2$	68
A.7	Discretization of $\nabla_x \tilde{\mu}$ and $\nabla_y \tilde{\mu}$ for J_x	69
A.8	Discretization of $\nabla_x \tilde{\mu}$ and $\nabla_y \tilde{\mu}$ for J_y	69
A.9	Microstructure generated using Voronoi tessellation.	70

Introduction

Today's electronic chips contain billions of transistors which are interconnected by multilayers of thin-film wires. With the miniaturization of electronic devices demand of smaller chips and narrower interconnects has increased and this is a real concern for the chip manufacturer as narrow interconnects have serious reliability issues. Typical current density often exceeds $10^6 A/cm^2$ and under such high current density atoms migrate in the direction of electron flow due to momentum transfer by the colliding electrons. This creates vacancies and these vacancies coalesce together to form a stable void. Once a void forms, it will migrate towards the cathode by diffusion of atoms through the easy diffusive paths along the surface of the void. Without any back stress this void grows with time[1] and ultimately leads to circuit failure. This mechanism of atom transport due to momentum transfer by electrons is known as **electromigration**.

Very high current density leads to joule heating in the interconnects. The device working temperature is kept around $100^\circ C$ with proper cooling arrangement. But, in some specific areas (hot spots) temperature can rise much higher than device working temperature. With the increase in temperature diffusivity of the atom increases which in-turn increases the rate of atom transfer due to electromigration. Current crowding occurs near the junctions of interconnect and contact via. Due to this high current flow in a small region, joule heating is pronounced. Excessive joule heating at the corners produce a temperature gradient from the corners to the bulk of the interconnect where temperature is more or less uniform. The temperature gradient can easily go upto $1000^\circ C/m$, which is sufficient enough for **thermomigration** to occur. Atoms start to migrate due the temperature gradient, the direction of motion varies with different elements, as copper(Cu) atoms move from hot to cold junction, tin(Sn) atoms move toward hot junction. Therefore, thermomigration also helps in void formation inside the interconnects.

The microstructure of the thin films are polycrystalline in nature. The grain boundaries provide another favourable diffusion path other than surface. So, the grain size distribution and the grain boundary network is also an important factor in electromigration. A grain boundary which is parallel to the current flow direction provides an easy pathway for atoms to migrate, whereas, a perpendicular grain boundary resists the atom migration towards anode. Apart from void formation, surface hillock formation is another reliability issue. When a grain boundary meets a free surface it forms a groove. Due to the electric current flow groove profile becomes unsymmetrical, a hillock forms on the anode side whereas a mass depletion occurs on the cathode side. The hillock grows with time as more and more atoms are deposited on it. This hillock can touch another nearby interconnect and lead to a short circuiting.

Stress is another factor in electromigration induced void evolution. Shape and size of the void is readily affected by stress. But, due to the vastness of the study of stress effects it is not explored in this work. This thesis is organized as follows: chapter 2 presents a brief overview of the literature on electromigration and thermomigration and a brief discussion on earlier works on these topics. Chapter 3 presents the details of the phase-field formulation for void migration under electric current and the details of introducing anisotropy in the surface energy and diffusivity. Next, a multi-phase field model is discussed to capture the physics of grain boundary grooving in a two grain system and coupled electromigration and thermomigration in a polycrystalline microstructure. Results and discussion part is divided in three chapters as void evolution (chapter 4), grain boundary grooving (chapter 5) and thermomigration (chapter 6), respectively. Chapter 7 concludes this thesis with a summary.

Literature Review

2.1 Electromigration

The concept of atom transport due to momentum transfer of electrons can be understood by a simple ballistic model[2]. The forces acting on an atom can be divided into two parts as direct force and wind force. ZeE is the direct force acting on an ion inside

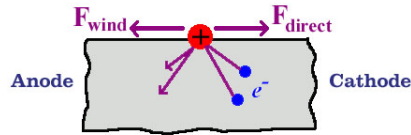


Figure 2.1: Forces on an ion inside a conductor.

an electric field of strength E . Wind force is defined as the force acting on an ion due to electrons hitting the ion, it can be expressed as $Z_{wd}eE$, where Z_{wd} is the charge number representing the momentum transfer by the electrons. These two forces are acting opposite to each other. So, we can represent the effective force on an diffusing ion as follows:

$$F_{em} = Z_{wd}eE + ZeE = Z^*eE \quad (2.1)$$

where Z^* represents the effective charge number for electromigration, here $Z^* < 0$.

Thin-film interconnects are deposited on a substrate and on the top of this a passive oxide layer is deposited. The top layer produces a compressive stress on the film. Residual stresses and high current flowing through the conductor help to nucleate void and grow. When atoms are moving towards anode they are producing compressive stress at the anode, so there is a stress gradient along the line. This gradient drives the vacancies toward the compressive region. So, if the length of the interconnect is small then the stress gradient can be substantial to prevent void coalescence. The critical length of interconnect which prevent voiding is known as **Blech length**. Though for

an infinitely long conductor the stress effect is negligible.

2.2 Grain boundary grooving

When a grain boundary touches a free surface it makes a groove in order to achieve a capillary force balance. The groove root makes an equilibrium dihedral angle determined by the ratio of grain boundary energy and surface energy. The semi-dihedral angle is given by Young's equation

$$\cos \theta = \frac{\gamma_{gb}}{2\gamma_s} \quad (2.2)$$

The groove deepens with time which provides a classic example of curvature driven mass transport. The mass flow out of the groove can occur by different mechanisms such as surface diffusion, grain boundary diffusion or evaporation-condensation mechanism. The groove profile is symmetrical on both side of the groove root. W. W. Mullins[3] has given an analytical solution to this problem considering evaporation-condensation mechanism and surface diffusion mechanism separately.

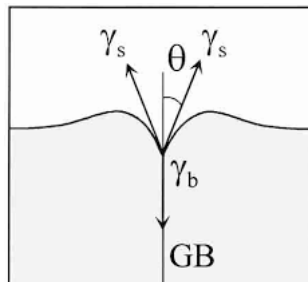


Figure 2.2: Grain boundary groove profile due to curvature driven mass transport.

In the presence of electric current the groove profile becomes unsymmetrical. An additional mass transport occurs along the surface due to electromigration which opposes the curvature driven flow in the cathode side. On the cathode side the groove surface becomes flat and on the other hand electromigration helps the curvature driven flow on the anode side, helping the anode side hillock formation. M. Ohring[4] proposed an analytical solution to this problem and showed the unsymmetrical groove profile.

Grain boundary groove can affect the grain boundary migration and grain growth in the thin films. Grain boundaries which are perpendicular to the groove sticks to the groove because to move the grain boundary it has to increase its length which is not energetically favourable. But, if the angle increases beyond a certain value then the

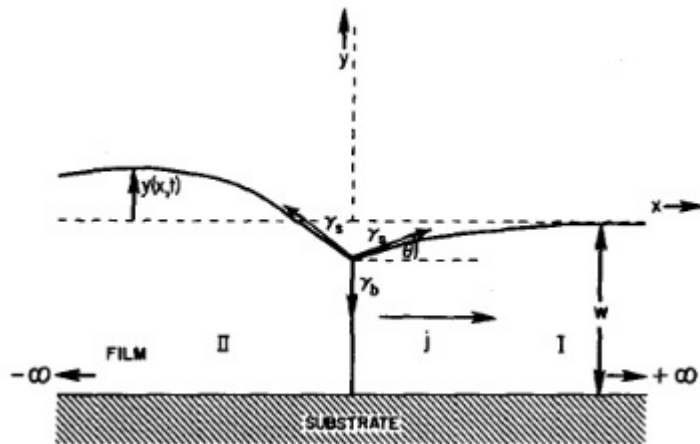


Figure 2.3: Grain boundary groove profile in the presence of electric current flowing from left to right[4].

boundary can break out from the groove and migrate. The calculation of critical angle and the velocity of migration has been done by Mullins[5]. Due to electric current flow, the grain boundary starts to bend and when the angle increases grain boundary starts to migrate. This phenomenon will be discussed in a later chapter.

2.3 Thermomigration

Thermomigration, commonly known as Soret effect or Ludwig-Soret effect was first observed in liquid mixtures where bigger particles move toward cold junction and smaller particles move toward hot junction under a temperature gradient. Binary alloys show prominent microstructural change under temperature gradient. Although, thermomigration in Al or Cu interconnects has seldom been studied, in reality there is always an effect of thermomigration in the electromigration induced void formation at cathode. Prominent joule heating occurs at the corners or bends of the complicated electronic circuit, whereas the temperature in the bulk remains constant. This provides a temperature gradient from the corners to the bulk. Fig.[2.4] shows the current crowding near the corners where the current enters or goes out of the interconnect and Fig.[2.5] shows a simplified temperature profile along the X-direction. The Driving

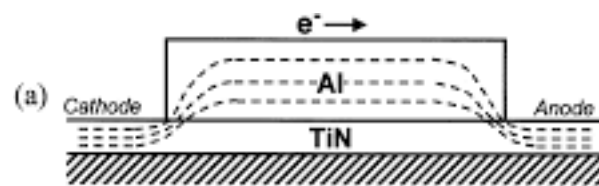


Figure 2.4: Current crowding at the corners[7].

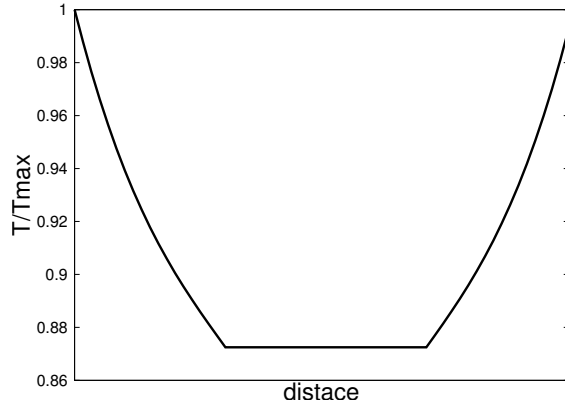


Figure 2.5: Typical temperature profile due the current crowding.

force for thermomigration is given as

$$F_{thermo} = -\frac{Q^*}{T} \nabla T \quad (2.3)$$

where Q^* is known as heat of transport. In comparison to the electromigration driving force where the effective charge number Z^* is generally negative for all elements in solid state, Q^* is positive for an element which moves from hot to cold end and Q^* is negative for an element which moves from cold to hot end. So, for the temperature profile shown above, the thermomigration force adds to the electromigration force on the cathode side and opposes the electromigration force on the anode side for the elements with positive Q^* .

2.4 Basic equations

Atoms move from the high diffusion potential to low diffusion potential area. For a curved void the diffusion potential changes as per the Gibbs-Thompson equation. The total driving force should be equal to the energy associated with the surface.

$$(c_v^{eq} - c_s^{eq})(\mu - \mu_{eq}) = \gamma \kappa \quad (2.4)$$

where μ_{eq} is the diffusion potential for flat interface, γ is the surface energy, κ is the curvature. Electric potential and temperature gradient add to the driving force for atom diffusion. The driving force for the flux of atoms is the gradient of effective diffusion potential($\tilde{\mu}$):

$$J = MF = -M \nabla \tilde{\mu} \quad (2.5)$$

where

$$\nabla \tilde{\mu} = -(2\Omega \nabla \mu + eZ^* E - \frac{Q^*}{T} \nabla T) \quad (2.6)$$

Eq.(2.3) follows the mass conservation. The surface normal velocity relates to the flux as follows:

$$v_n = -\Omega \frac{\partial J}{\partial s}$$

2.5 Phase field model

Phase field model is basically a diffuse interface model. The interfaces have a definite width and the phase field variables change continuously across the width. In this way we can eliminate the singularities associated with the sharp interface model. In this model we do not need to track the interface explicitly. The free energy of the system is defined in terms of the phase field variables and the system will tend to lower its free energy and as a result microstructure evolves with morphological changes in different phases. Broadly, two types of phase field equations are there, one is Cahn-Hilliard equation which uses a conserved order parameter to define the phase field; on the other hand Allen-Cahn equation which uses a non-conserved order parameter to define the phase field. Allen-Cahn equation coupled with mass conservation equation can describe the general moving boundary problems where mass is also conserved.

2.5.1 Phase field model of electromigration

In recent years phase field model has gained its popularity among the researchers. It has a range of applications from solidification to solid state phase transformations, from crack propagation to grain growth and recently in biological systems. Initial works on electromigration were based on finite element methods, then Mahadevan and Bradley[6] published their work based on Cahn-Hilliard model considering electric effect only, Bhate et al.[8] added the stress effect in the Cahn-Hilliard model, then Barrett et al. published a phase field model for electromigration induced intergranular void. In our model we have used the Allen-Cahn equation using a non-conserved order parameter coupled with a mass conservation equation. The driving force for the

evolution of phase field variable is formulated by grand potential formulation[9].

2.5.2 Phase field model of thermomigration

Very few works have been done on thermomigration in the interconnects, most of the studies have been done for flip chip solder joints. Recently, Somaiah et. al.[10] showed the effect of electric current induced thermal gradient on the mass transport in the interconnects. Mohanty et. al.[11] studied the diffusion under thermal gradient using a cahn-Hilliard phase field model. Zhang et. al.[12] used a Cahn-Hilliard phase field model to simulate pore migration under thermal gradient coupled with heat transfer. Therefore, we tried to match the experimental results found by Somaiah et. al. in the same multi-phase field formulation used for electromigration adding a temperature gradient in the system.

Model Formulation

3.1 Isotropic formulation

This work is based on the Allen-Cahn type dynamics using a non-conserved order parameter to formulate the free energy functional. This equation is then coupled with a mass conservation equation. With this model we have successfully simulated the void motion and its corresponding shape and size change. The model formulation starts with taking a simple double obstacle potential $f_0 = 9\phi^2(1 - \phi)^2$ which has a non-zero value only at the interface. The evolution equation for ϕ is the following:

$$\tau\epsilon\frac{\partial\phi}{\partial t} = -(\gamma\epsilon(\frac{\partial f_o}{\partial\phi}) - 2(\gamma/\epsilon)\nabla^2\phi) - \Delta\psi\frac{\partial h(\phi)}{\partial\phi}. \quad (3.1)$$

where the last term represents the driving force for electromigration. The driving force $\Delta\psi$ can be calculated by grand chemical potential formulation[9].

$$\Delta\psi = \psi^s - \psi^v$$

$$\Delta\psi = (c_v^{eq} - c_s^{eq})(\mu - \mu_{eq}) \quad (3.2)$$

Substituting the expression for $\Delta\psi$ in the evolution equation we get

$$\tau\epsilon\frac{\partial\phi}{\partial t} = -(\gamma\epsilon(\frac{\partial f_o}{\partial\phi}) - 2(\gamma/\epsilon)\nabla^2\phi) - (c_v^{eq} - c_s^{eq})(\mu - \mu_{eq})\frac{\partial h(\phi)}{\partial\phi}. \quad (3.3)$$

We chose the interpolating function $h(\phi)$ such that:

$$h(\phi) = \phi^2(3 - 2\phi) \quad (3.4)$$

$$\frac{\partial h(\phi)}{\partial \phi} = 6\phi(1 - \phi)$$

The local composition can be written as:

$$c = c_v(1 - h(\phi)) + c_s h(\phi) \quad (3.5)$$

here, c_v and c_s represent the composition of void and solid, respectively.

composition of void and solid can be represented as a function of μ such that :

$$c_v(\mu) = \mu \quad (3.6)$$

$$c_s(\mu) = k\mu + \mu_0 \quad (3.7)$$

where k and μ_0 are constants. Now, the mass conservation equation can be written as:

$$\frac{\partial c}{\partial t} = \nabla \cdot (M \nabla \tilde{\mu}) \quad (3.8)$$

where

$$\tilde{\mu} = 2\Omega\mu + eZ^*V \quad (3.9)$$

is the driving force for mass transport, and Ω is the atomic volume, eZ^* is the effective charge for electromigration and V is the electric potential.

As there is no charge accumulation inside the conductor the electric potential can be calculated using Laplace equation :

$$\nabla \cdot (\zeta(\phi) \nabla V) = 0 \quad (3.10)$$

where $\zeta(\phi)$ represents the variation of permittivity through the bulk and the void. This can be written as:

$$\zeta(\phi) = \zeta_s \phi + \zeta_v (1 - \phi) \quad (3.11)$$

where ζ_s and ζ_v represent permittivity in the solid and the void, respectively. Now, considering equation 2.9 again we can formulate the evolution equation for μ as:

$$\frac{\partial c}{\partial \mu} \frac{\partial \mu}{\partial t} + \frac{\partial c}{\partial \phi} \frac{\partial \phi}{\partial t} = \nabla \cdot (M \nabla \tilde{\mu})$$

$$\frac{\partial \mu}{\partial t} = \frac{\nabla \cdot (M \nabla \tilde{\mu}) - \frac{\partial c}{\partial \phi} \frac{\partial \phi}{\partial t}}{\frac{\partial c}{\partial \mu}} \quad (3.12)$$

where M is a phenomenological term which can be written in terms of diffusivity as:

$$M = \frac{D}{2\Omega} \frac{\partial c}{\partial \mu} \quad (3.13)$$

We are considering surface diffusion only, so to make diffusivity non-zero only at the interface we will multiply D with $\phi(1 - \phi)$.

So, we have three equations which need to be solved sequentially:

$$\nabla \cdot (\zeta(\phi) \nabla V) = 0$$

$$\tau \epsilon \frac{\partial \phi}{\partial t} = -(\gamma \epsilon \left(\frac{\partial f_o}{\partial \phi} \right) - 2(\gamma/\epsilon) \nabla^2 \phi) - (c_v^{eq} - c_s^{eq})(\mu - \mu_{eq}) \frac{\partial h(\phi)}{\partial \phi}$$

$$\frac{\partial \mu}{\partial t} = \frac{\nabla \cdot (M \nabla \tilde{\mu}) - \frac{\partial c}{\partial \phi} \frac{\partial \phi}{\partial t}}{\frac{\partial c}{\partial \mu}}$$

3.2 Implementing anisotropy

3.2.1 Anisotropic diffusivity

Diffusivity in tensorial form: Diffusivity is a second rank tensor which relates to vector quantities as follows:

$$\begin{Bmatrix} j_x \\ j_y \end{Bmatrix} = - \begin{bmatrix} D_{xx} & D_{xy} \\ D_{yx} & D_{yy} \end{bmatrix} \begin{Bmatrix} \nabla_x \tilde{\mu} \\ \nabla_y \tilde{\mu} \end{Bmatrix}$$

In principle form this tensor can be written as:

$$D = \begin{bmatrix} D_{\perp} & 0 \\ 0 & D_{\parallel} \end{bmatrix}$$

Now, this matrix should be transformed into the coordinate system of void, which can be performed as:

$$\begin{bmatrix} D_{xx} & D_{xy} \\ D_{yx} & D_{yy} \end{bmatrix} = RDR^{-1} \quad (3.14)$$

where R is the transformation matrix which is represented as:

$$R = \begin{bmatrix} \cos \theta & -\sin \theta \\ \sin \theta & \cos \theta \end{bmatrix}$$

We have given a four fold anisotropy to the component D_{\parallel} . It can be represented as following:

$$D_{\parallel} = D(1 + \delta \cos(4\theta)) \quad (3.15)$$

where D is the isotropic diffusivity and δ is the strength of anisotropy. The angle θ can be expressed in terms of surface normal \vec{n} as $\theta = \tan^{-1} \left(\frac{n_x}{n_y} \right)$.

So, $\cos \theta = n_x$, $\sin \theta = n_y$, $\vec{n} = n_x \vec{i} + n_y \vec{j}$, $n_x^2 + n_y^2 = 1$.

Now, \vec{n} can be written as $\vec{n} = \frac{\nabla \phi}{|\nabla \phi|}$, $n_x = \frac{(\partial \phi)}{(\partial x)}$, $n_y = \frac{(\partial \phi)}{(\partial y)}$.

We need to expand the $\cos(4\theta)$ term completely in terms of gradients of ϕ . The

following scheme is adopted:

$$\cos(4\theta) + i \sin(4\theta) = (\cos \theta + i \sin \theta)^4$$

Equating the real parts,

$$\begin{aligned} \cos(4\theta) &= \cos^4 \theta + \sin^4 \theta - 6 \cos^2 \theta \sin^2 \theta \\ &= 4(\cos^4 \theta + \sin^4 \theta) - 3(\cos^2 \theta + \sin^2 \theta)^2 \\ &= 4(\cos^4 \theta + \sin^4 \theta) - 3 \\ &= 4(n_x^4 + n_y^4) - 3 \\ &= 4 \left(\frac{\phi_x^4 + \phi_y^4}{|\nabla \phi|^4} \right) - 3 \end{aligned}$$

Here $\phi_x = \left(\frac{\partial \phi}{\partial x} \right)$ and $\phi_y = \left(\frac{\partial \phi}{\partial y} \right)$.

So, the anisotropic diffusivity takes the form as:

$$D_{\parallel} = D \left(1 + \delta \left(4 \left(\frac{\phi_x^4 + \phi_y^4}{|\nabla \phi|^4} \right) - 3 \right) \right) \quad (3.16)$$

The components in the transformed coordinate become dependent on both D_{\perp} and D_{\parallel} as follows:

$$\begin{aligned} D_{xx} &= D_{\perp} \cos^2 \theta + D_{\parallel} \sin^2 \theta = D_{\perp} \left(\frac{\phi_x^2}{|\nabla \phi|^2} \right) + D_{\parallel} \left(\frac{\phi_y^2}{|\nabla \phi|^2} \right) \\ D_{xy} &= D_{yx} = \sin \theta \cos \theta (D_{\perp} - D_{\parallel}) = \left(\frac{\phi_x \phi_y}{\phi_x^2 + \phi_y^2} \right) (D_{\perp} - D_{\parallel}) \\ D_{yy} &= D_{\perp} \sin^2 \theta + D_{\parallel} \cos^2 \theta = D_{\perp} \left(\frac{\phi_y^2}{|\nabla \phi|^2} \right) + D_{\parallel} \left(\frac{\phi_x^2}{|\nabla \phi|^2} \right) \end{aligned}$$

3.2.2 Anisotropic surface energy

To implement anisotropy in surface energy we adopted a four fold cubic anisotropy similar to diffusivity.

$$a_c(\theta) = (1 + \delta_{\gamma} \cos(4\theta)) \quad (3.17)$$

$$\gamma = \gamma_0 a_c(\theta) \quad (3.18)$$

But for the case of surface energy anisotropy we need to consider the Gibbs-Thompson effect and to consider the effect of anisotropy we will introduce the term

surface stiffness(Ψ) in place of surface energy.

$$\Psi = \gamma + \frac{\partial^2 \gamma}{\partial \theta^2} \quad (3.19)$$

$$\Psi = \gamma_0 (1 - 15\delta_\gamma \cos(4\theta)) \quad (3.20)$$

Considering “weak anisotropy” where $\delta_\gamma < 1/15$, the surface stiffness term is always positive.

$$\mu = \mu_{eq} - \Omega \Psi \kappa \quad (3.21)$$

Like diffusivity, anisotropic surface energy can be expressed completely in terms of gradients of ϕ .

$$\gamma = \gamma_0 \left(1 + \delta_\gamma \left(4 \left(\frac{\phi_x^4 + \phi_y^4}{|\nabla \phi|^4} \right) - 3 \right) \right) \quad (3.22)$$

As surface energy contributes to the free energy we need to modify our free energy functional to incorporate anisotropy.

$$F = \int_{-\infty}^{\infty} (\gamma_0 a_c^2(\theta) |\nabla \phi|^2 + \frac{\gamma_0}{\epsilon} 9\phi^2(1-\phi)^2 + \dots) dx \quad (3.23)$$

The variational derivative operator expands as,

$$\frac{\delta}{\delta \phi} = \left(\frac{\partial}{\partial \phi} - \nabla \cdot \frac{\partial}{\partial \nabla \phi} \right)$$

Then on incorporating anisotropy, the gradient energy term in the evolution equation gets modified to,

$$\frac{\delta}{\delta \phi} (a_c^2 |\nabla \phi|^2) = \frac{\partial}{\partial \phi} (a_c^2 |\nabla \phi|^2) - \nabla \cdot \frac{\partial}{\partial \nabla \phi} (a_c^2 |\nabla \phi|^2)$$

As a_c and $\nabla \phi$ both depends on ϕ_x and ϕ_y , the first term in the derivative vanishes to zero. Also, in Cartesian coordinates $\frac{\partial}{\partial \nabla \phi}$ can be written as,

$$\frac{\partial}{\partial \nabla \phi} = \frac{\partial}{\partial \phi_x} \hat{i} + \frac{\partial}{\partial \phi_y} \hat{j}$$

So, the evolution equation for ϕ becomes,

$$\tau\epsilon \frac{\partial \phi}{\partial t} = \gamma_0 \epsilon \nabla \cdot \left(\begin{array}{c} \frac{\partial}{\partial \phi_x} (a_c |\nabla \phi|^2) \\ \frac{\partial}{\partial \phi_y} (a_c |\nabla \phi|^2) \end{array} \right) - \frac{\gamma_0}{\epsilon} 18\phi(1-\phi)(1-2\phi) + (k-1)\mu(\mu - \mu_{eq}) 6\phi(1-\phi)$$
(3.24)

where the terms inside the divergence can be expanded as following:

$$\begin{aligned} \frac{\partial}{\partial \phi_x} (a_c |\nabla \phi|^2) &= 2a_c \phi_x \gamma_0 \left(1 - \frac{16\delta_\gamma(\phi_x^2 \phi_y^2 - \phi_y^4) + 4\delta_\gamma(\phi_x^4 + \phi_y^4)}{(\phi_x^2 + \phi_y^2)^2} + 3\delta_\gamma \right) \\ \frac{\partial}{\partial \phi_y} (a_c |\nabla \phi|^2) &= 2a_c \phi_y \gamma_0 \left(1 - \frac{16\delta_\gamma(\phi_x^2 \phi_y^2 - \phi_x^4) + 4\delta_\gamma(\phi_x^4 + \phi_y^4)}{(\phi_x^2 + \phi_y^2)^2} + 3\delta_\gamma \right) \end{aligned}$$

3.3 Multi-phase field model

In the practical world the class of materials we consider are generally consist of multiple phases and multiple components. The interfaces between different phases play an important role in microstructure evolution like grain growth, grain boundary grooving etc. Whereas, multiple components give rise to complex phase diagrams, co-existence of multiple phases play an important part in the alloy solidification and solid state phase transformations. So, to understand the physics behind all these transformations we need to treat all the phases and its interfaces separately. Multi-phase field models have been developed by some of the researchers[13, 14] to model the practical problems of material science. In this section, we are going to discuss one of the multi-phase field models which we have implemented in our model.

We have used a grand potential multi-phase field model developed recently by Choudhury and Nestler[9]. A system of N phases have been considered where the phases may represent different orientation of grains, different properties of grains, different compositions etc. A phase field order parameter is defined as $\phi = (\phi_1, \phi_2, \dots, \phi_N)$ which is continuous throughout the domain. The ϕ_α represent the state of the phase α , where the each ϕ_α continuously varies between 0 and 1. The model requires another constraint of

$$\sum_{\alpha=1}^N \phi_\alpha = 1.$$

The evolution equation of each N phases ϕ_α follows the similar equation as mentioned earlier in this chapter,

$$\tau\epsilon \frac{\partial \phi}{\partial t} = \epsilon \left(\nabla \cdot \frac{\partial a(\phi, \nabla \phi)}{\partial \nabla \phi_\alpha} - \frac{\partial a(\phi, \nabla \phi)}{\partial \phi_\alpha} \right) - \frac{1}{\epsilon} \frac{\partial w(\phi)}{\partial \phi_\alpha} - \frac{\partial \Psi(\mu, \phi)}{\partial \phi_\alpha} - \lambda \quad (3.25)$$

the only new thing added is the Lagrange parameter “ λ ” to maintain the constraint of $\sum_{\alpha=1}^N \phi_\alpha = 1$. We can define the whole right hand side portion of the Eq.[3.25] other than λ as rhs_α . The constraint of $\sum_{\alpha=1}^N \phi_\alpha = 1$ requires that $\sum_{\alpha=1}^N \frac{\partial \phi}{\partial t} = \sum_{\alpha=1}^N (rhs_\alpha - \lambda) = 0$. So, λ is calculated from

$$\lambda = \frac{1}{N} \sum_{\alpha=1}^N rhs_\alpha \quad (3.26)$$

The gradient energy density $a(\phi, \nabla \phi)$ for a isotropic case can be written in terms of a generalized antisymmetric gradient vector

$$a(\phi, \nabla \phi) = \sum_{\alpha < \beta}^N \gamma_{\alpha\beta} (\vec{q}_{\alpha\beta})^2 \quad (3.27)$$

where $\vec{q}_{\alpha\beta}$ is a normal vector to the $\alpha\beta$ interface, $\vec{q}_{\alpha\beta} = (\phi_\alpha \vec{\nabla} \phi_\beta - \phi_\beta \vec{\nabla} \phi_\alpha)$. The potential part of the interfacial free energy density $w(\phi)$ can be chosen as multi-well or multi-obstacle potential. The advantage of choosing a obstacle potential over the well type potential is that the partial differential equations only need to be solved at certain places so it is computationally efficient. We have chosen a double obstacle potential with higher order terms,

$$w(\phi) = \frac{16}{\pi^2} \sum_{\alpha < \beta}^N \gamma_{\alpha\beta} \phi_\alpha \phi_\beta + \sum_{\alpha < \beta < \delta}^N \gamma_{\alpha\beta\delta} \phi_\alpha \phi_\beta \phi_\delta \quad (3.28)$$

where the higher order term $\gamma_{\alpha\beta\delta} \phi_\alpha \phi_\beta \phi_\delta$ is added to avoid any third phase occurrence at the two phase interfaces. The value of $\gamma_{\alpha\beta\delta}$ is chosen to be $\approx 10\gamma_{\alpha\beta}$. But, the ϕ_α can rise or fall to any value if we do not impose the criteria that $w(\phi)$ is valid only inside a domain, elsewhere it is infinity. So we define a Gibbs simplex $\Sigma = \phi_\alpha \geq 0 \forall \phi_i$ and $\sum_{i=1}^N \phi_i \leq 1$. So, we need to impose the Gibbs simplex and correct the ϕ_α values after each time evolution step.

Now for the grand potential $\Psi(\phi)$ part we need to choose the bulk free energy

terms for all the phases. For our model we have chosen an ideal solution model for bulk free energy functions. First, we will define concentration of a component in a two component system, here we will take $c = c^{atom}$. The free energy density function looks like the following:

$$f^\alpha = c^\alpha \ln c^\alpha + (1 - c^\alpha) \ln(1 - c^\alpha) + Bc^\alpha + C \quad (3.29)$$

where B and C are two constants. By taking derivative with respect to c^α we will get the equation for μ ,

$$\mu = \frac{\partial f^\alpha}{\partial c^\alpha} = \ln \left(\frac{c_\alpha}{1 - c^\alpha} \right) + B \quad (3.30)$$

and from the equation for μ we will get the equation for c^α which will be back substituted to the eq.[3.29],

$$c^\alpha = \frac{\exp^{(\mu-B)}}{1 + \exp^{(\mu-B)}}. \quad (3.31)$$

Now, the grand potential for the phases are formulated as[9],

$$\Psi^\alpha = f^\alpha - \mu c^\alpha. \quad (3.32)$$

To formulate the grand potential for the system we will interpolate the Ψ^α 's with a proper interpolating function,

$$\Psi = \sum_{\alpha=1}^N \Psi^\alpha h_\phi^\alpha \quad (3.33)$$

where $h_\phi^\alpha = (\phi^\alpha)^2(3 - 2\phi^\alpha) + 2\phi^\alpha\phi^\beta\phi^\delta$ interpolates between all the phases and also satisfy $\sum_{\alpha=1}^N h_\phi^\alpha = 1$.

Similarly, the mass conservation equation is modified for multi-phase field model, here the evolution of composition is now calculated for each component and the mobility of the interface is taken as a weighted value of mobility in all the phases. for our case we have only one component for which we will track the composition. The mass

conservation equation becomes

$$\frac{\partial c}{\partial t} = \nabla \cdot (M(\phi) \nabla \mu), \quad (3.34)$$

where

$$M(\phi) = \sum_{\alpha=1}^N M^\alpha h_\phi^\alpha, \quad (3.35)$$

where each of the M^α is related to diffusivity as

$$M^\alpha = D^\alpha \frac{\partial c^\alpha}{\partial \mu}. \quad (3.36)$$

Results and Discussions

Void Evolution in Presence of Electric Current

4.1 Defining parameters

For our simulation we have used finite difference for discretization all the equations. A 100×100 mesh-grid with $\Delta x = \Delta y = 1$ is taken for all the simulations. We used $\Delta t = 0.005$ for a stable numerical calculation. The relaxation parameter τ is taken as 1 and ϵ which is related to the interface width, should be taken small to adequately approximate the reality but also it should be taken large enough to remove the singularities across the interfaces, so it is taken as 3.0. The permittivity of void and solid is taken as 1 and 5 respectively. The morphological changes associated with the void have different driving forces: void growth, migration and void shape is determined by the interplay between the surface energy and electric current. So, we have defined a non-dimensional parameter χ which represents this interplay between the driving forces.

$$\chi = \frac{e|Z^*|Er^2}{\Omega\gamma} \quad (4.1)$$

When χ is small it means the driving force for electromigration is small compared to the surface energy, so the void will maintain its shape. When the value is on higher side, the void shape changes because the electromigration force takes over the surface energy. From now we will compare our simulation results on the basis of this parameter.

For the electric potential we have implemented constant boundary condition for all the boundaries of mesh-grid, so, a constant potential difference is maintained across the line. We kept the potential for cathode at zero and varied the anode potential. For the phase field variable ϕ and diffusion potential μ we have imposed no-flux boundary

condition.

4.2 1D results

Using the 1D simulation we have checked the void migration towards cathode and the electric potential distribution across the line. We have found electric potential changes linearly.

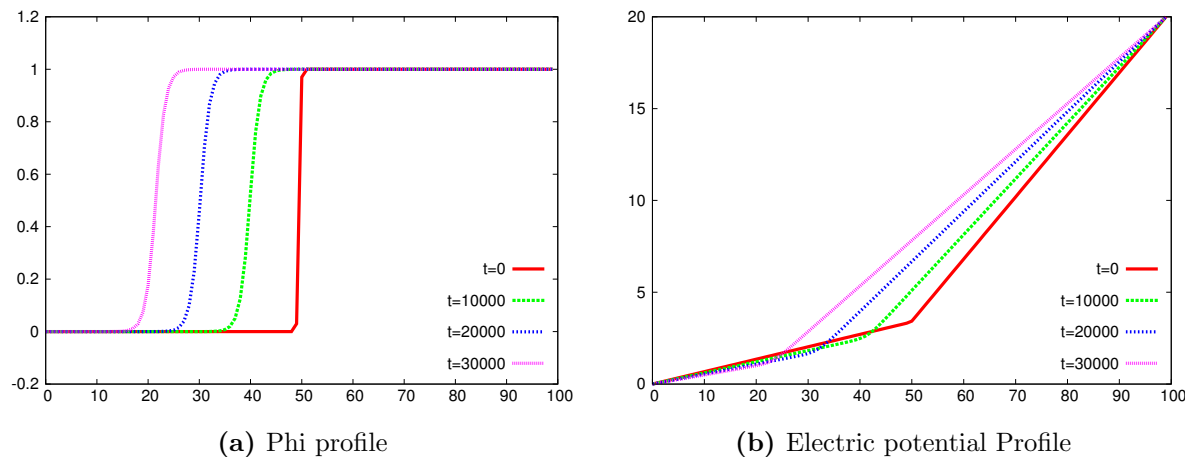


Figure 4.1: (a) ϕ profile where $\phi = 0$ is void and $\phi = 1$ is solid;(b) electric potential profile where left terminal is cathode(-ve) and right terminal is anode(+ve).

4.3 2D results

In this work we considered only surface diffusion driven morphological changes. So, to restrict any bulk diffusion contribution we multiplied D with $\phi(1 - \phi)$, this will restrict the diffusion only through the void surface. For 2D simulation we need to consider the Gibbs-Thompson effect, we calculated μ with which we initialized our system. $(c_v^{eq} - c_s^{eq})(\mu - \mu_{eq}) = \gamma\kappa$, where $\mu_{eq} = 0$ and c_v^{eq} and c_s^{eq} is zero and 1 respectively. So, we can write $\mu_{initial} = -\frac{\gamma}{r}$ as curvature in 2D can be written as $\frac{1}{r}$ where “r” is radius of the void.

4.3.1 Isotropic case

A void of radius $r = 7.0$ is taken for all the simulations. The initial state is shown in the following figure:

The simulation results for $\chi = 1.225$ is shown in Fig.[4.3], it can be inferred that void growth as well as migration is sluggish. Void shape remains circular due to lack of electromigration driving force. The top of the void from where the atoms are removed

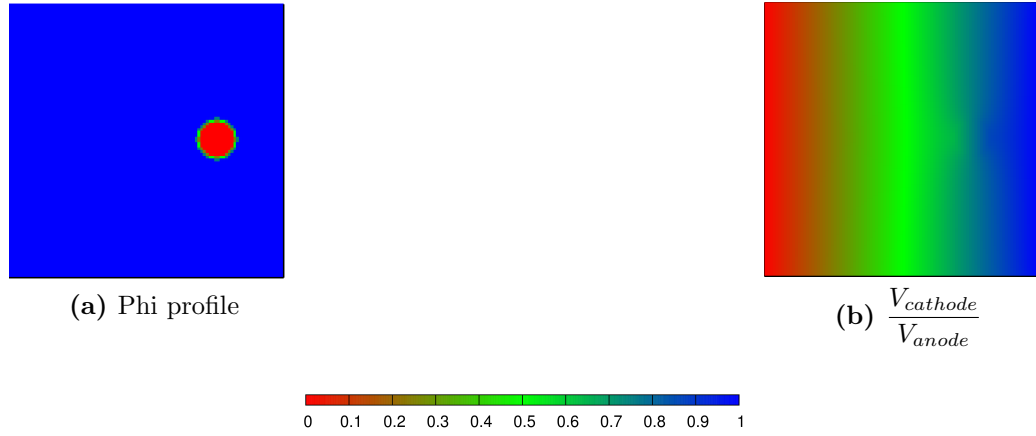


Figure 4.2: Initial condition for all the cases.

is filled by atoms coming from cathode side by the diffusion process, it is mostly a steady state growth. A nucleated void inside an interconnect in this regime or lower takes much longer time to grow and cause circuit failure. As, χ is non-dimensional parameter it can be used to calculate the safe operating condition for a given void size.

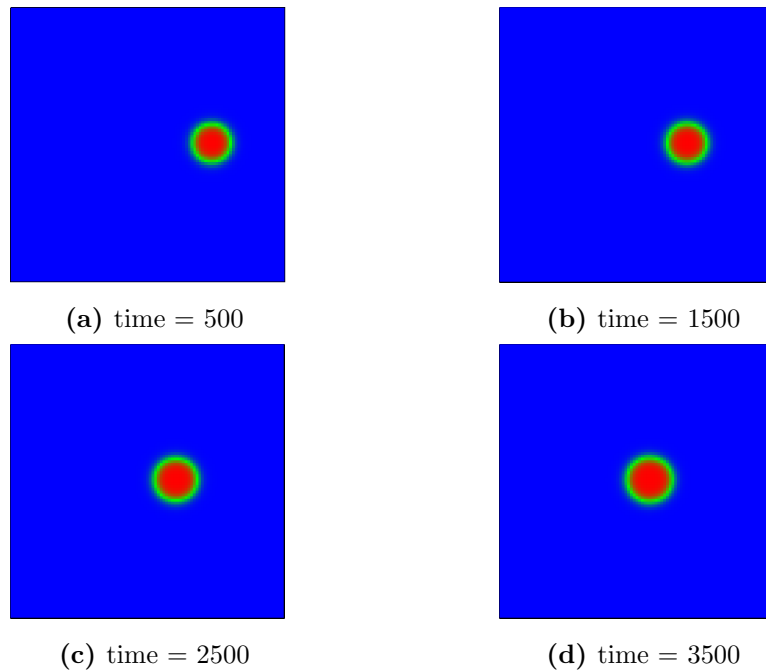


Figure 4.3: simulation results for $\chi = 1.225$.

Next, simulations have been done with $\chi = 2.45$ which is twice of the previous value. In the Fig.[4.4] we can see that void growth and migration is much faster than the previous case. Surface energy term is not dominating, so, the shape is not circular any more.

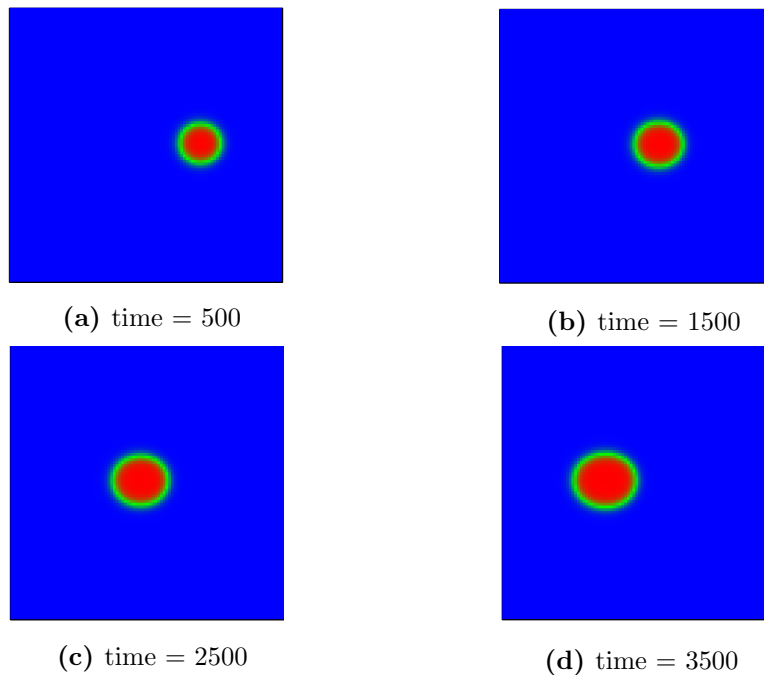


Figure 4.4: simulation results for $\chi = 2.45$.

With the value of $\chi = 4.9$ Fig.[4.5], the electromigration driving force is so large that it produces a condition for instability. The front which is facing the electrons grows rapidly. This regime of void growth is really unsafe and the circuit fails after a short time.

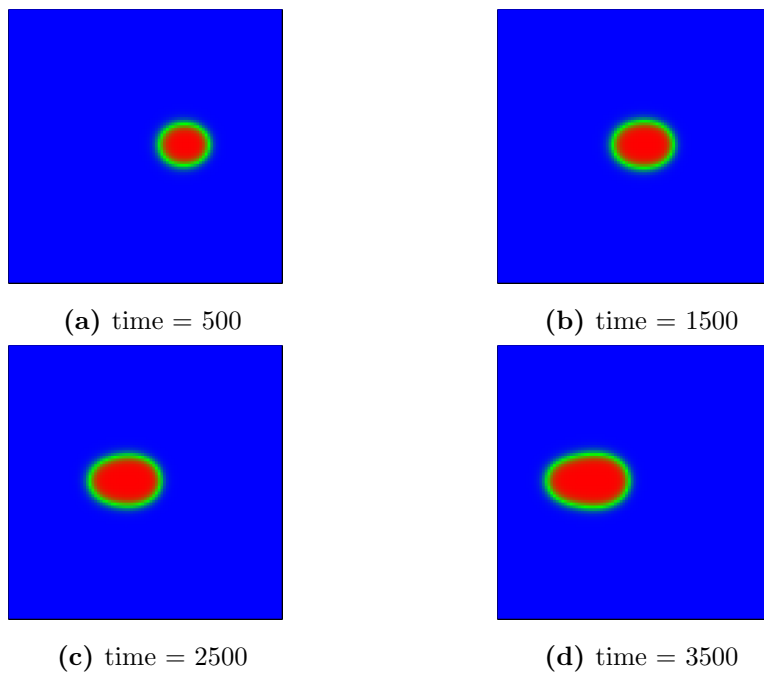
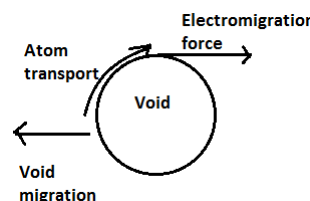


Figure 4.5: simulation results for $\chi = 4.9$.

The physics behind this can be explained as following:



Due to electromigration of atoms from the top of the void surface there will a gra-

dient in effective diffusion potential. Atoms will move from the cathode side of the void to the top under this gradient of effective diffusion potential. Now this gradient depends on the potential difference across the line. So, for small potential difference the gradient is small and the atom flows steadily along the void surface maintaining its shape. But, when the gradient is high, atom transport will be very fast from the cathode side of void, creating an instability on the cathode side. The void gets elongated to lower the gradient in effective diffusion potential.

We have plotted the volume of void vs. time for different χ values Fig.[4.6(a)]. It can be observed that after an initial transient period the void volume increases linearly with time. The analytical solution for void volume change is available[1], our results matches the analytical solution. Experiments were done to track the resistance change in the interconnect and the resistance change is also found to be linearly proportional to time. Resistance is an indicator of void volume.

$$V = \frac{eZ^*EDAt}{kT}$$

To understand the shape change associated with the void we plotted the c/a ratio with the time, where c is the major axis and a is the minor axis and for perfect circle $c/a = 1$. It is observed that small values of χ the ratio remains close to 1, but as χ increases the ratio increases. In Fig.[4.7] the front velocity of void is plotted for different χ value. From this plot we can infer that the velocity is linearly proportional to the parameter χ , that means velocity increases linearly with increasing the electromigration driving force. This relationship can also be established analytically[16].

$$v_n = \frac{M\Omega e Z^* E}{r} = \frac{M\gamma\Omega}{r^3} \chi$$

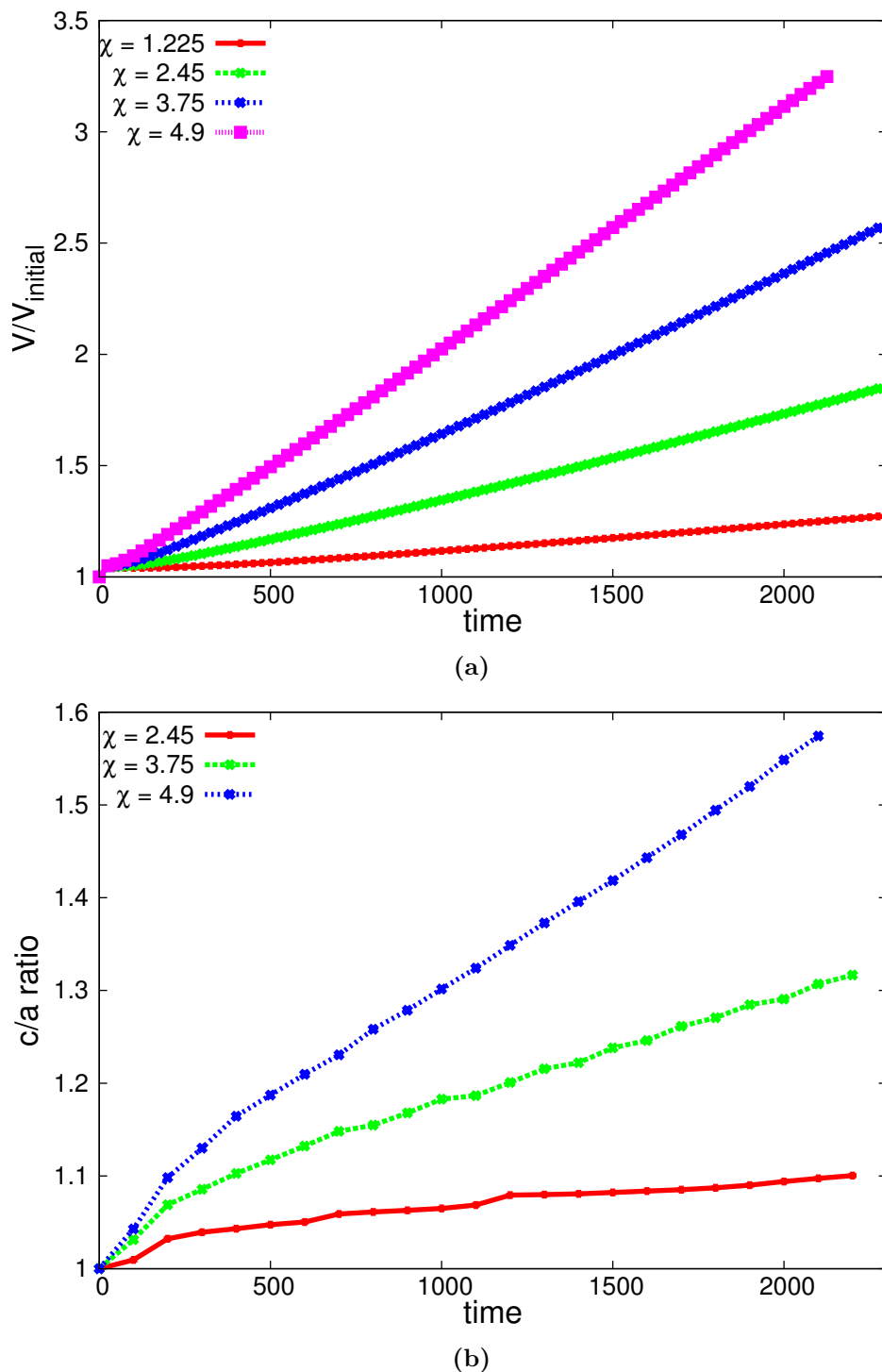


Figure 4.6: (a) simulation results for void volume increase with time for different χ values, (b) void shape change with time for different χ .

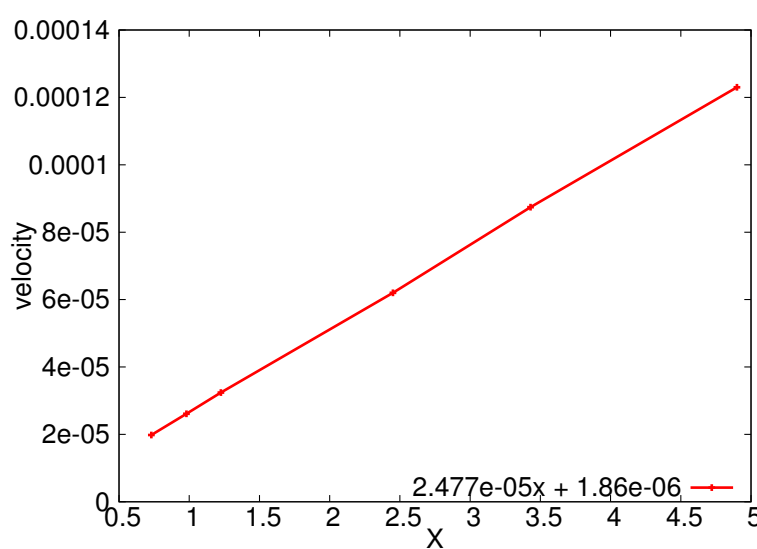


Figure 4.7: Front velocity of void vs. χ .

4.3.2 Anisotropic surface energy

We have introduced a cubic anisotropy for the surface energy term. The circular shape changes to equilibrium wulff shape for cubic system. The equilibrium shape takes up those planes which have the lowest surface energy. We have taken the value of $\delta_\gamma = 0.05$, which is representing the weak anisotropy.

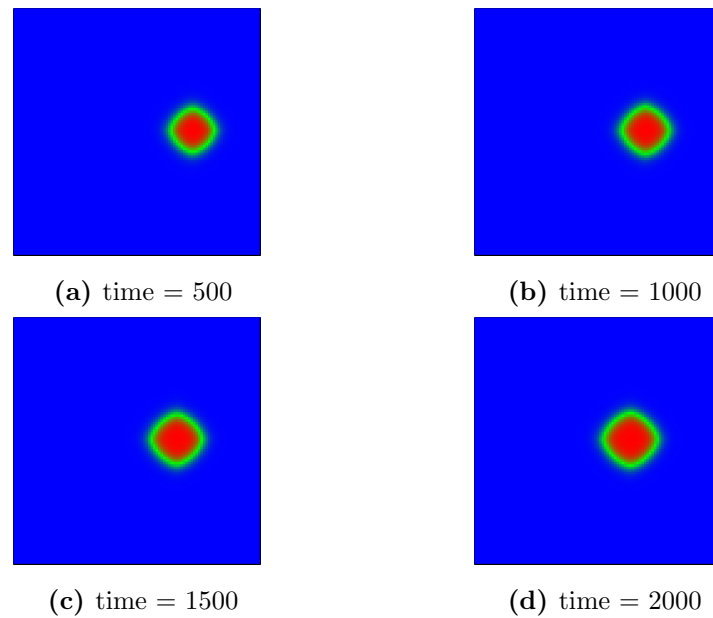


Figure 4.8: simulation results with anisotropic surface energy for $\chi = 0.98$.

For small value of χ the void preserves its shape. With the increase in the electromigration driving force the volume increment is much higher but the shape of void remains intact.

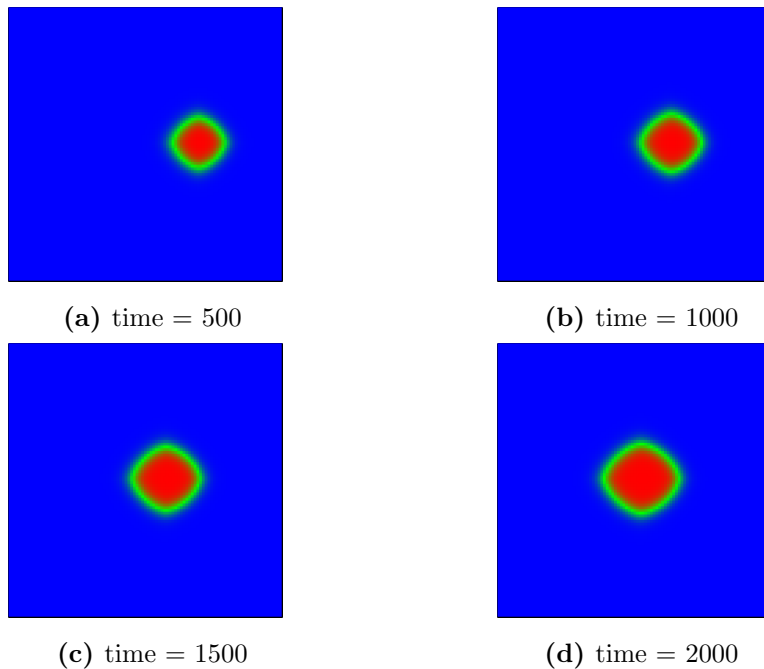


Figure 4.9: simulation results with anisotropic surface energy for $\chi = 1.96$.

Comparing the results for $\chi = 4.9$ with the isotropic case we can observe that for anisotropic case the wulff shape remains intact but it gets elongated along the x-axis.

The surface energy contribution is still dominating on the shape of void.

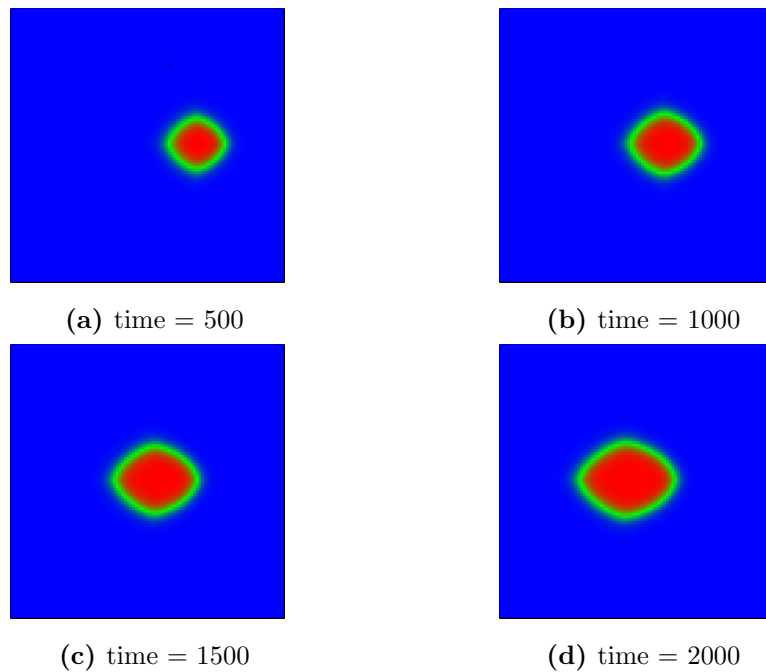


Figure 4.10: simulation results with anisotropic surface energy for $\chi = 4.9$.

4.3.3 Diffusivity anisotropy

There are several materials in which surface diffusivity varies with the orientation, the activation energy in different planes can vary by a large amount. Similar to the anisotropic surface energy, diffusivity anisotropy can also lead to faceted void shape. Sometimes, the effect of diffusivity anisotropy is much larger than anisotropic surface energy. As discussed in chapter 3, the anisotropic term δ can have very small to very high value. We simulated our system using a constant potential difference as $\chi = 1.96$. We varied the value of δ from very small to high values. For smaller values the shape change is not prominent, but with increasing anisotropy the void takes a four fold faceted shape with slight distortion. The distortion is because of atomic flux from left to right side. It can be inferred that the void takes up those planes where diffusivity is the lowest, because the slowest diffusivity paths will determine the actual diffusion rate.

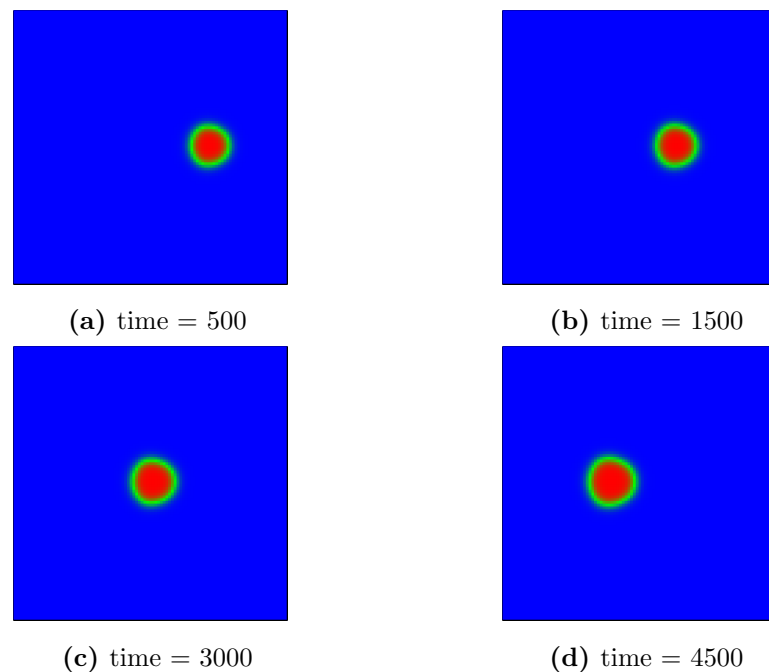


Figure 4.11: Anisotropic diffusivity strength $\delta = 0.35$.

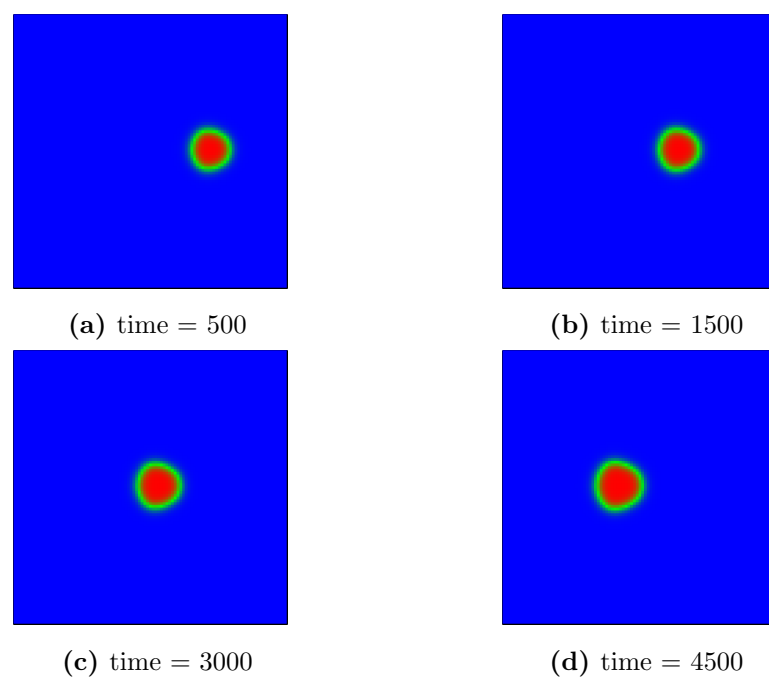


Figure 4.12: Anisotropic diffusivity strength $\delta = 0.5$.

Grain Boundary Grooving and Effect of Electric Current

This chapter deals with the classic problem of grain boundary grooving and the effect of electric current on the groove profile. The multi-phase field model has been utilized to simulate the grooving dynamics and the results have been matched with analytical solution proposed by W. W. Mullins[3]. After benchmarking with analytical solution we have extended our model to incorporate the effect of electric current on grooving dynamics. Unsymmetrical grooving and grain boundary migration have been observed. Next, 3D simulations with multiple grains have been done to observe the pit formation at grain boundary triple junctions.

5.1 2D simulation of grain boundary grooving

5.1.1 Model system

Two 100×50 grid sized grains have been chosen to simulate the grooving of the grain boundary between them. Both the grains surrounded by a vapor phase on the top which is of 200×50 grid size. With $\Delta x = 20.0$, our system is of the size of 4000×2000 . the timestep is taken as $\Delta t = 0.3 \times 400$ for all the cases. For ϕ evolution equation we have applied no-flux boundary condition in X and Y-direction. The model system is shown in below:

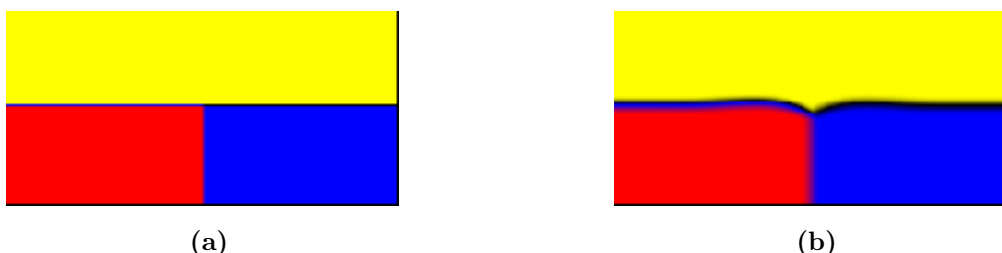


Figure 5.1: (a) Initial system, (b) after grooving.

5.1.2 Comparison with Mullins theory

We have considered mass transport only due to surface diffusion. Mullins, in his research paper[3], has given the equation for the evolution of groove profile due to surface diffusion. The analytical solution is the following:

$$\frac{\partial y}{\partial t} = -B \frac{\partial}{\partial x} \left[(1 + y'^2)^{-1/2} \frac{\partial}{\partial x} \left(\frac{y''}{(1 + y'^2)^{3/2}} \right) \right] \quad (5.1)$$

where, $y(x, t)$ is the groove profile for ($x \geq 0$) and $B = D_s \gamma \Omega^2 \nu / kT$ is a constant for a given condition. Mullins assumed a small slope approximation where $|y| \ll 1$ which is reasonable enough as the groove surface remains flat with respect to the original flat surface. The Eq.[5.1] then reduce to

$$\frac{\partial y}{\partial t} = -By''' \quad (5.2)$$

The analytical solution of the Eq.[5.2] is established by considering three boundary conditions:

$$\begin{aligned} (x, 0) &= 0, \\ y'(0, t) &= \tan(90 - \theta) = m, \\ y'''(0, t) &= 0. \end{aligned}$$

where θ is the semi-dihedral angle. The final solution is represented by a power series expansion as follows:

$$y(x, t) = m(Bt)^{1/4} Z \left[\frac{x}{(Bt)^{1/4}} \right] \quad (5.3)$$

where $Z(u)$ can be expressed as

$$Z(u) = \sum_{n=0}^{\infty} a_n u^n.$$

We have done our simulation taking a isotropic case of surface energy(γ_s) and grain boundary energy(γ_{gb}). The groove profile is shown in the following figure:

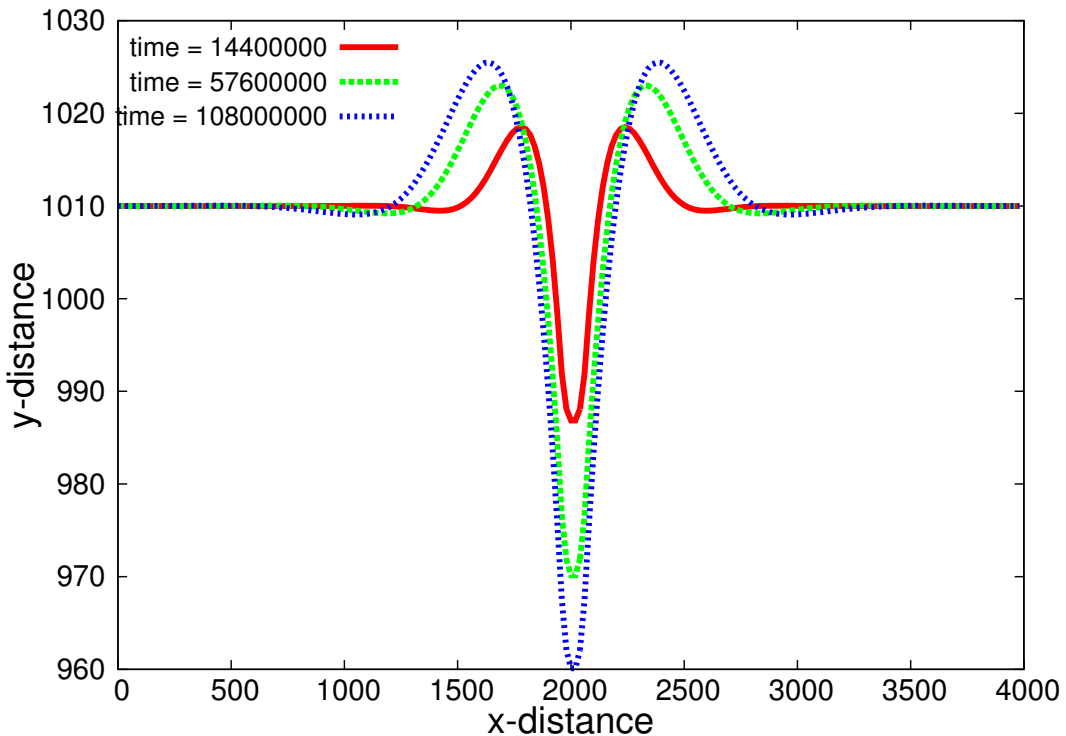


Figure 5.2: Groove profile for $\frac{\gamma_{gb}}{\gamma_s} = 1.0$ case for different timesteps.

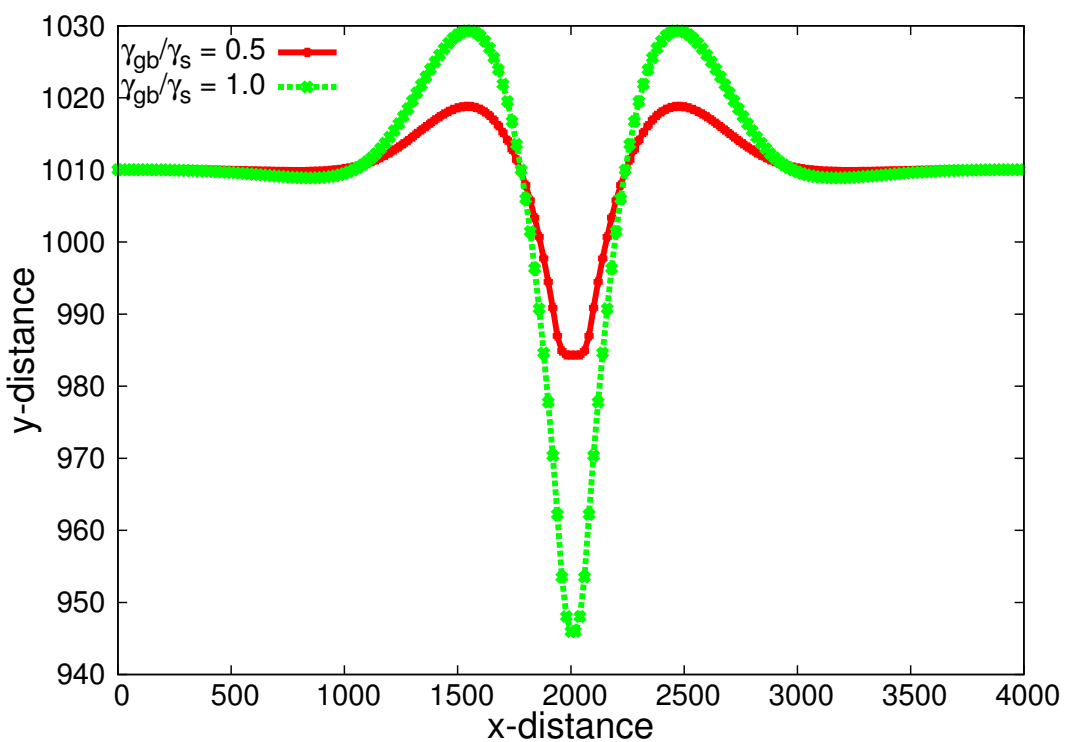


Figure 5.3: Groove profile for two different $\frac{\gamma_{gb}}{\gamma_s}$ ratio for same timestep.

The equilibrium dihedral angle is calculated after a very long timestep by fitting two polynomials for the left and right side of the groove profile respectively. The angle is calculated at the point of intersection for the polynomials using their slopes at that point. The depth of groove is also calculated from the intersection point of the two polynomials.

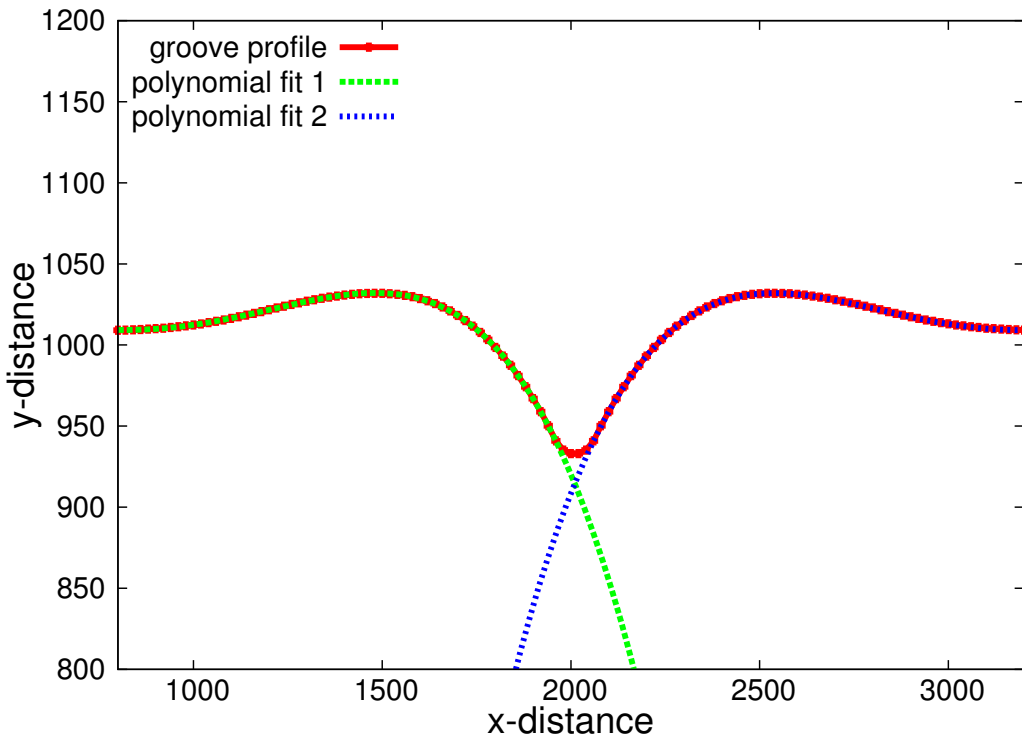


Figure 5.4: Measuring groove angle by fitting two polynomials for $\frac{\gamma_{gb}}{\gamma_s} = 1.0$ case.

case	surface energy(γ_s)	grain boundary energy(γ_{gb})	$\theta = \cos^{-1}\left(\frac{\gamma_{gb}}{2\gamma_s}\right)$	θ from simulation
I	1.0	1.0	60°	59.89°
II	1.0	0.5	75.52°	75.46°

Table 5.1: Comparison of equilibrium semi-dihedral angle and simulation semi-dihedral angle.

Eq.[5.1] is solved numerically taking $x = 0$ and $y(0,t)$ at the point where the two polynomials meet during curve fitting. The analytical profile matches well with our phase field simulation.

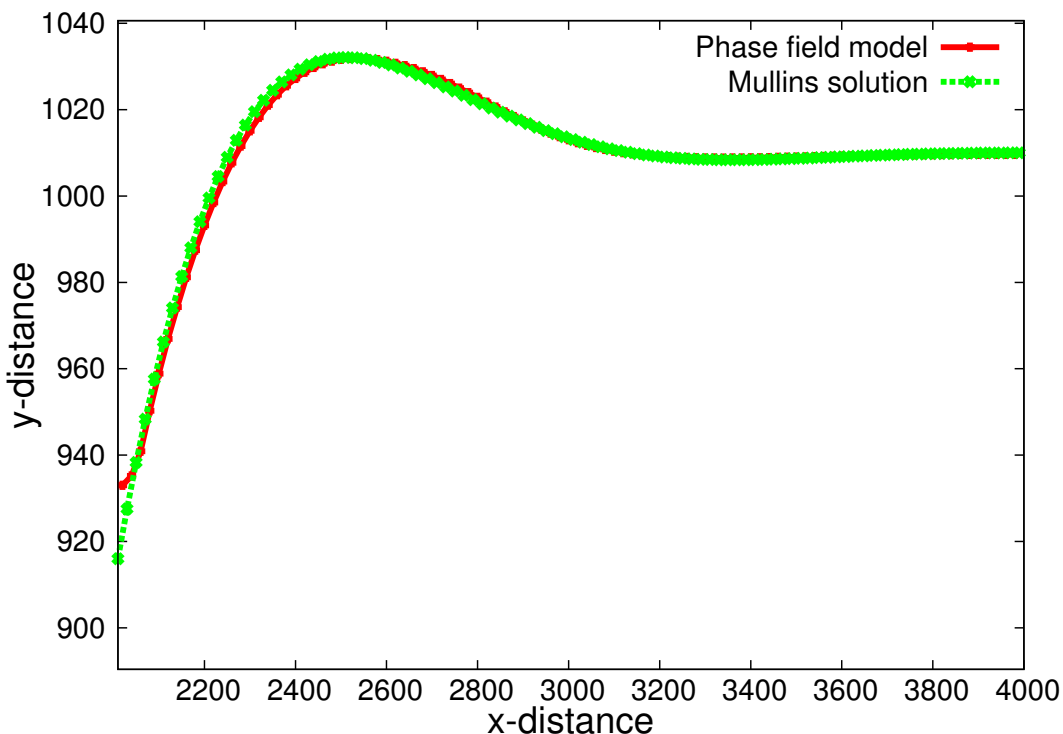


Figure 5.5: Comparison of the phase field model($\frac{\gamma_{gb}}{\gamma_s}=1.0$) with Mullins analytical solution.

We have extracted other information like groove depth(d_g) and hillock height(d_h) from our phase field model. Following Mullins theory we know that $d = d_g + d_h$, the distance from maximum of the surface to the grain boundary, varies with $t^{1/4}$, which actually is the case with our phase field simulation.

$$d = d_g + d_h = 0.973m(Bt)^{1/4} \quad (5.4)$$

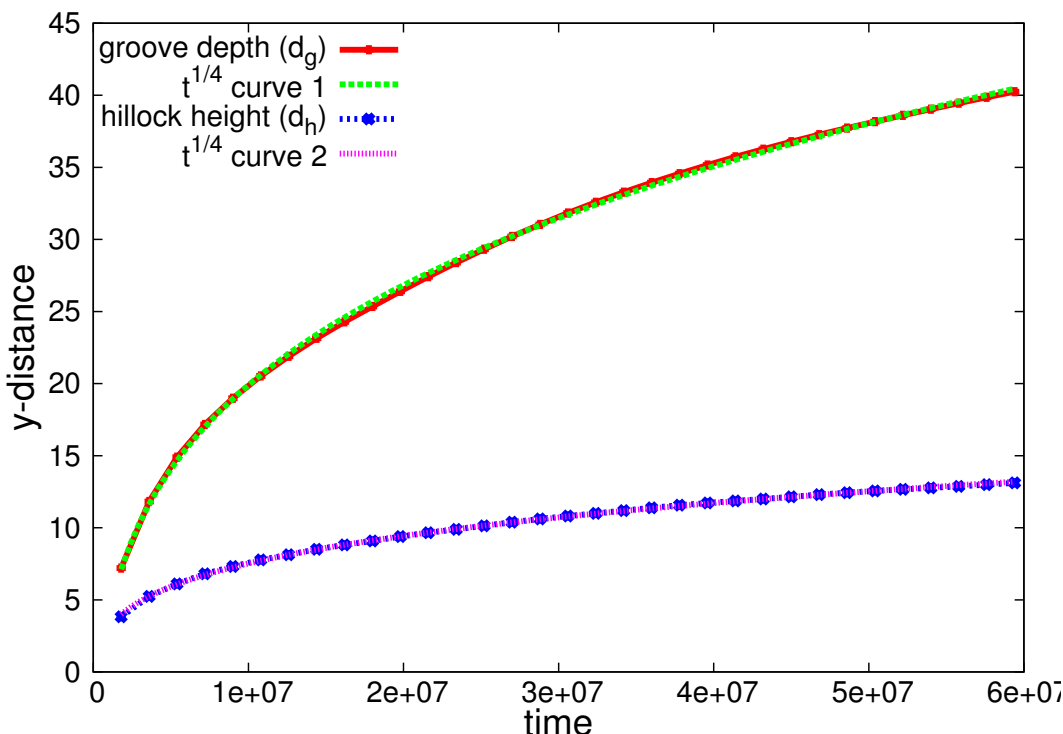


Figure 5.6: Groove depth and hillock height vs. time for $\frac{\gamma_{gb}}{\gamma_s}=1.0$.

Also, the separation between the two maxima varies with $t^{1/4}$, our phase field result also agrees well with this.

$$s = 4.6(Bt)^{1/4} \quad (5.5)$$

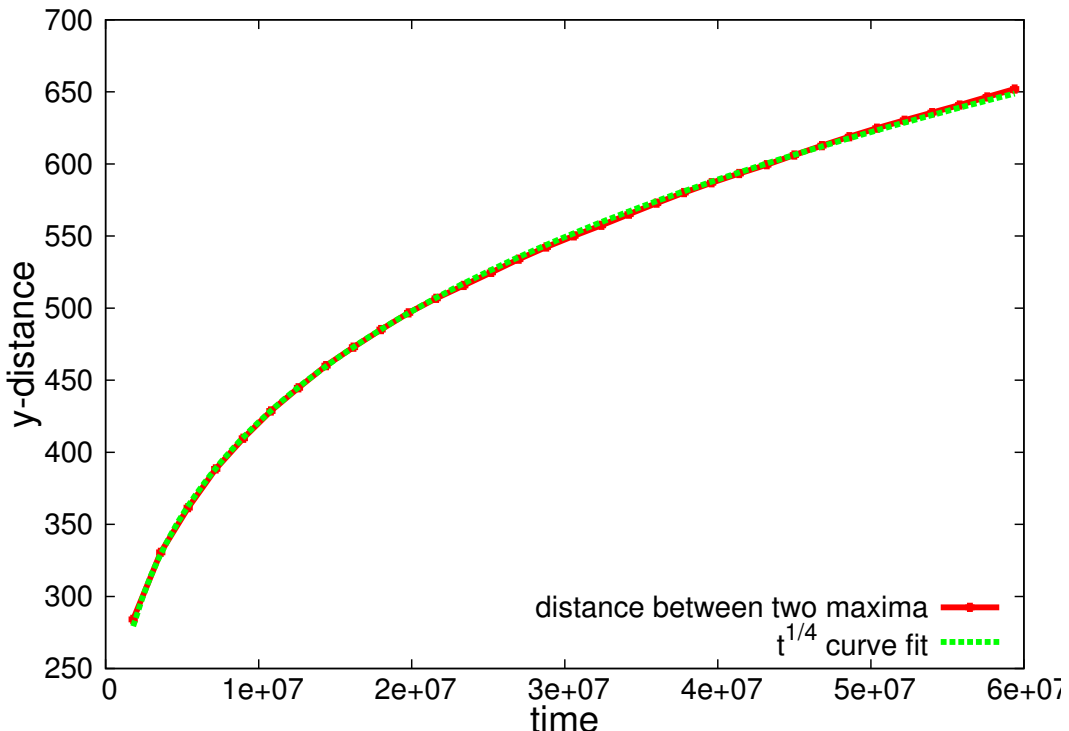


Figure 5.7: Separation between two hillocks vs. time for $\frac{\gamma_{gb}}{\gamma_s} = 1.0$.

5.2 3D simulation of grain boundary grooving

Once we have benchmarked our phase field model with Mullins analytical theory, we have extended our model in 3-dimensional system with hexagonal equiaxed grains. Pit formations have been observed at the grain boundary triple points which is consistent with the analytical study done by Genin et. al.[17].

5.2.1 Model system

A 3D system has been chosen with $(123 \times 100 \times 72)$ meshsize. $\Delta x = \Delta y = \Delta z = 30.0$ is chosen for all the simulations which implies to a total system size of $(3690 \times 3000 \times 2160)$. $\Delta t = 0.05 \times 900$ is chosen for all the simulations. The system has been filled with rectangular grains which become hexagonal after a few smoothing timesteps. Along half of the Y-axis it is solid phase and the other half is vapour phase. For ϕ evolution equation we have applied periodic boundary condition in the X and Z-direction, and no-flux boundary condition in Y-direction.

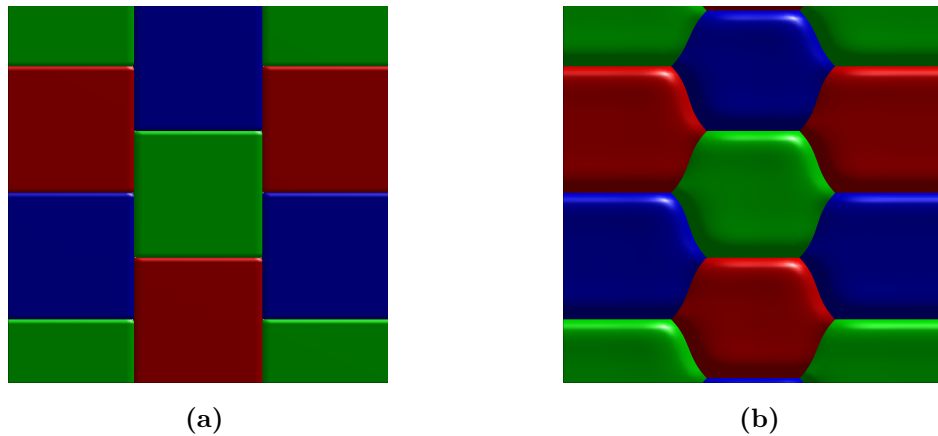
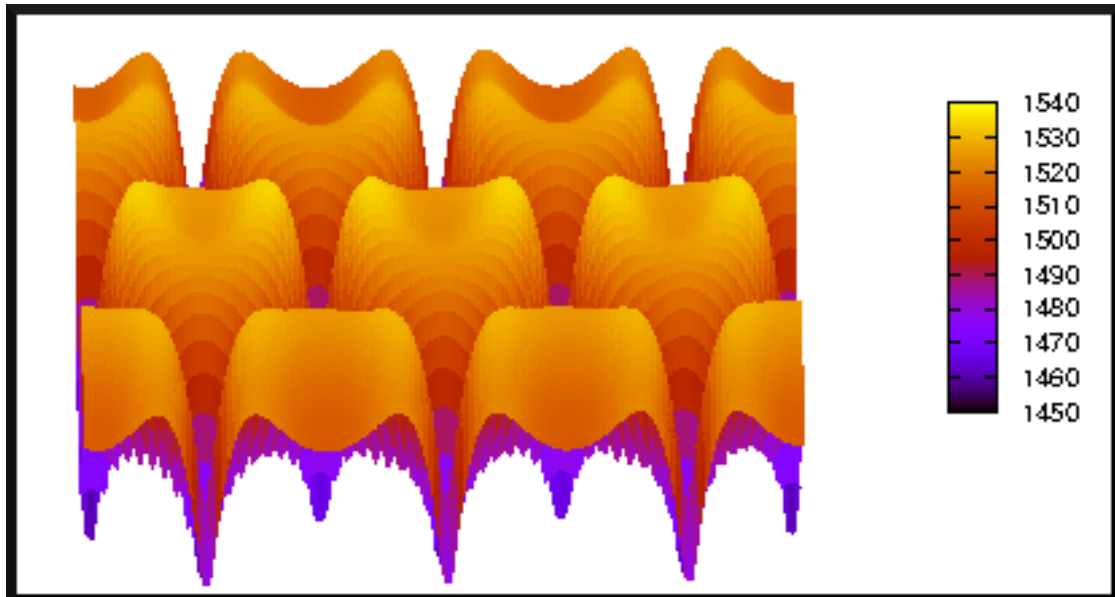


Figure 5.8: Surface Plot(X-Z plane) (a) initial system, (b) after smoothing steps.

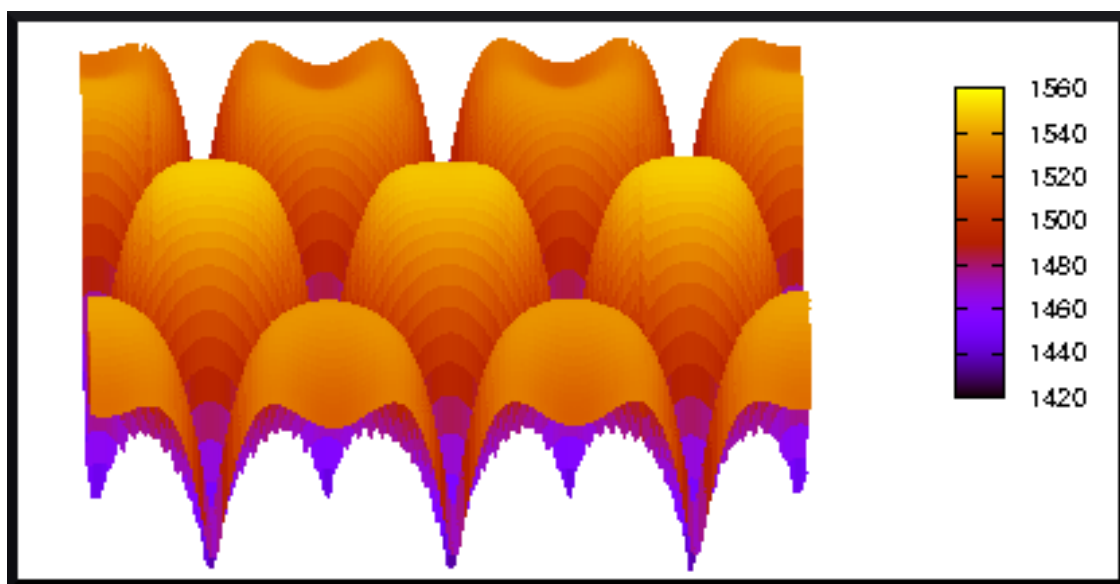
5.2.2 Pit formation at grain boundary vertices

Apart from grain boundary grooving, pits at the grain boundary vertices have been observed in our 3D simulations. The depth of these pits(d_p) are more than the groove depth(d_g). Genin et. al.[17] showed in their work that the pit depth follows the same $t^{1/4}$ dependence like grain boundary groove, along with this the slope around the pit is much steeper than around the grain boundary groove between two grains, which is the reason for pits around grain boundary triple points are much deeper than the grain boundary grooves along two grains. Therefore, these pits can penetrate much faster than the grain boundary grooves and make voids inside the polycrystalline thin film. Srolovitz et. al.[18] predicted that these pits are responsible for thin film breakup.

Groove depth and pit depth have been measured from our simulation results. d_p shows a $t^{1/4}$ time dependence, which matches well with the analytical solution provided by Genin et. al. Further, $\frac{d_p}{d_g}$ ratio has been measured for different timesteps. Genin et. al.[17] showed that the pit depth at origin is twice the depth of a groove far from the pit. Our measured $\frac{d_p}{d_g}$ ratio from simulation result approaches to this value.



(a) time = 13500000



(b) time = 40500000

Figure 5.9: Solid-vapour interface plot (x-z plane) for two different timesteps.

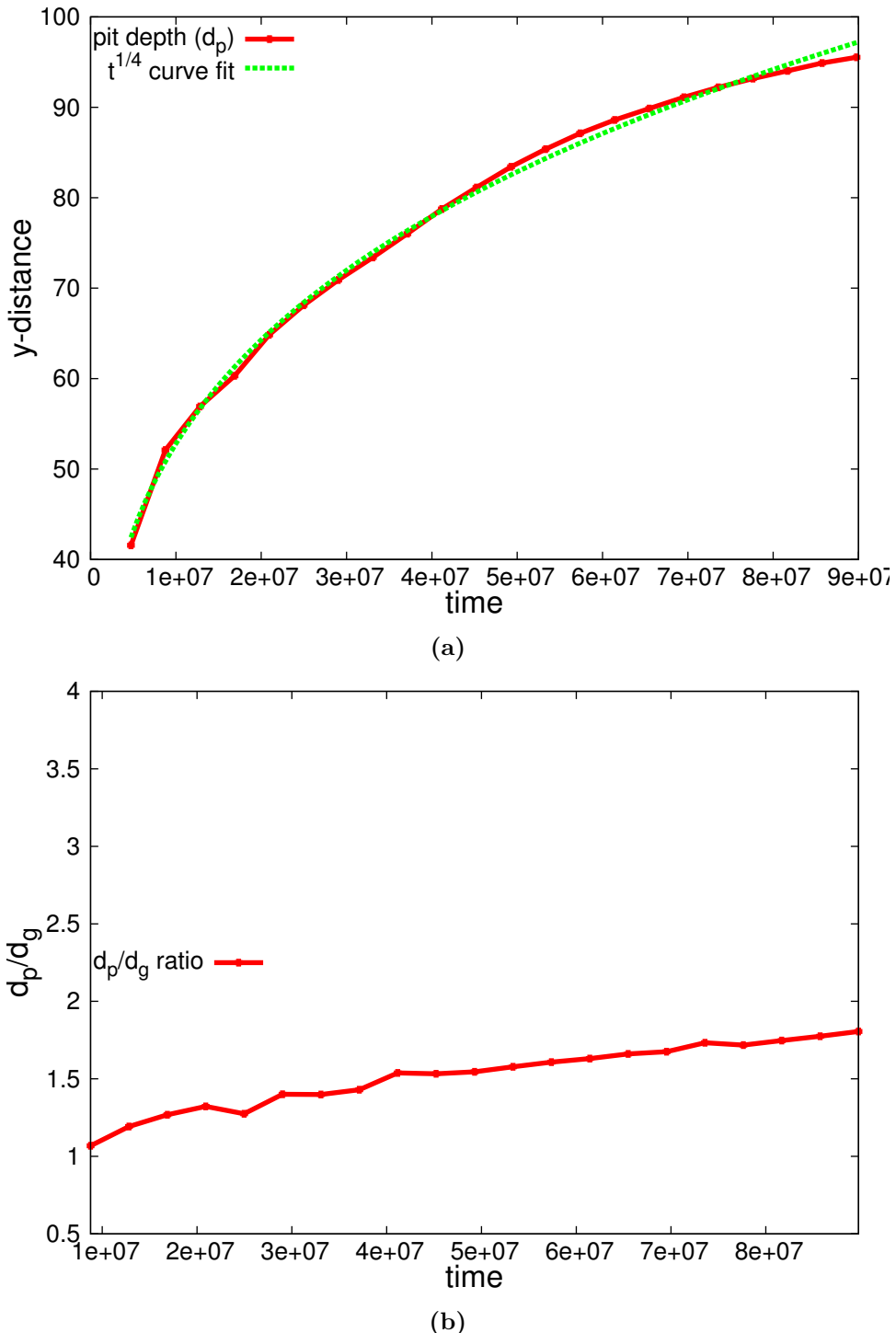


Figure 5.10: (a) Pit depth follows a $t^{1/4}$ time dependence, (b) d_p/d_g ratio ≈ 2 .

5.3 Effect of electric current on grain boundary grooving

This section deals with the effect of mass transport due to electric current on the grain boundary grooving dynamics. Thin film interconnects have great extent of free surfaces, so, surface grooving can play an important part in the reliability of the interconnects. In thermal grooving atoms move on both the direction of the groove, Where in the presence of high electric current atoms move from cathode to anode direction. As a result, mass flow due to electric current opposes the curvature driven

mass flow on the cathode side, while it assists the curvature driven mass flow on the anode side. Therefore, an unsymmetrical groove profile evolves with a flat surface on the cathode side and a hillock on the anode side. Experiments have been done to observe this unsymmetrical grooving, Rosenberg and Ohring produced some SEM images of Aluminum interconnect showing grain boundary hillocks and whisker [19].

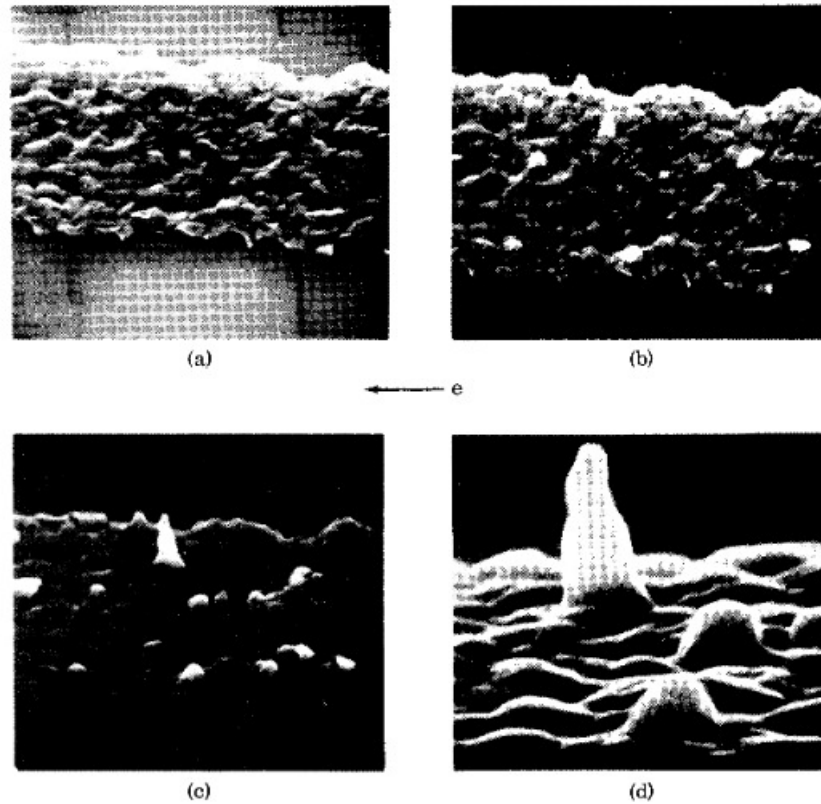


Figure 5.11: SEM images showing grain boundary hillocks and whisker around grain boundary holes[19], the arrow shows the direction of electron flow.

5.3.1 Grain boundary migration under electric current

Grain boundary migration and related grain growth has been observed in thin films due to electric current. But, this kind of grain growth is related to the grain boundary grooving phenomenon and thus it is observed in the grains near the surface. Mullins[5] in his work discussed about the effect of grain boundary grooving on grain boundary migration, it is shown that a grain boundary which is perpendicular to the the groove can not migrate but if the grain boundary exceeds a critical angle then the grain boundary starts migrating. In the case of electromigration, the equilibrium dihedral angle breaks instantaneously due the high wind force, to re-establish the equilibrium angle the groove root bends inside making a flat surface on the cathode side, hence, resulting the grain boundary to bow in the direction of anode. Mullins showed that a slight difference in surface curvature across the groove root may produce large driving force for boundary migration, while the grain boundary curvature itself play a minor

part in boundary migration. Genin[20] in his work has discussed about the grain boundary migration due to grooving under the effect of stress.

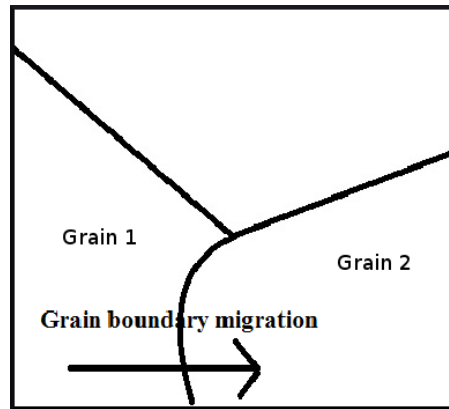


Figure 5.12: Schematic showing the grain boundary migration due to distorted groove root.

5.3.2 2D simulation results

The model system size is taken same as before, only the individual grain dimensions are changed to capture the grain boundary migration towards cathode side. The anode side grain is of (1000×1000) size and the cathode side grain is of (3000×1000) size. A electric potential difference has been applied across the X-direction. To solve the Laplace equation we have applied constant boundary condition in X-direction and no-flux in Y-direction.

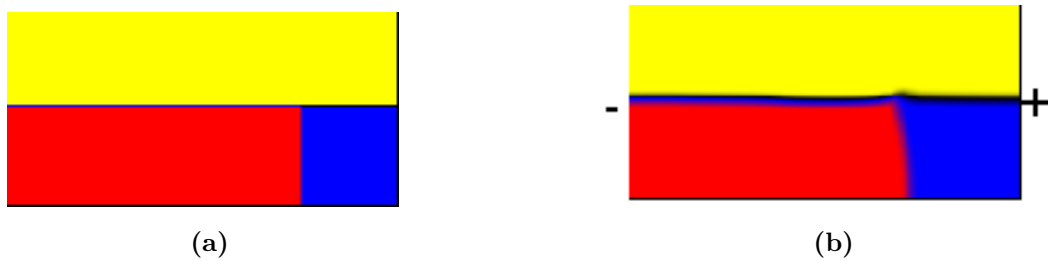


Figure 5.13: (a) Initial system (b) after applying electric current.

Groove profiles have been studied under various applied electric currents. It is found that initially the groove profile changes with time for all the applied electric currents, then after a period of time it takes the form of a ridge on the cathode side and on the anode side forms a hillock. From Fig.[5.14] it can be easily understood that groove profile takes a constant shape but the size of the groove increases with time.

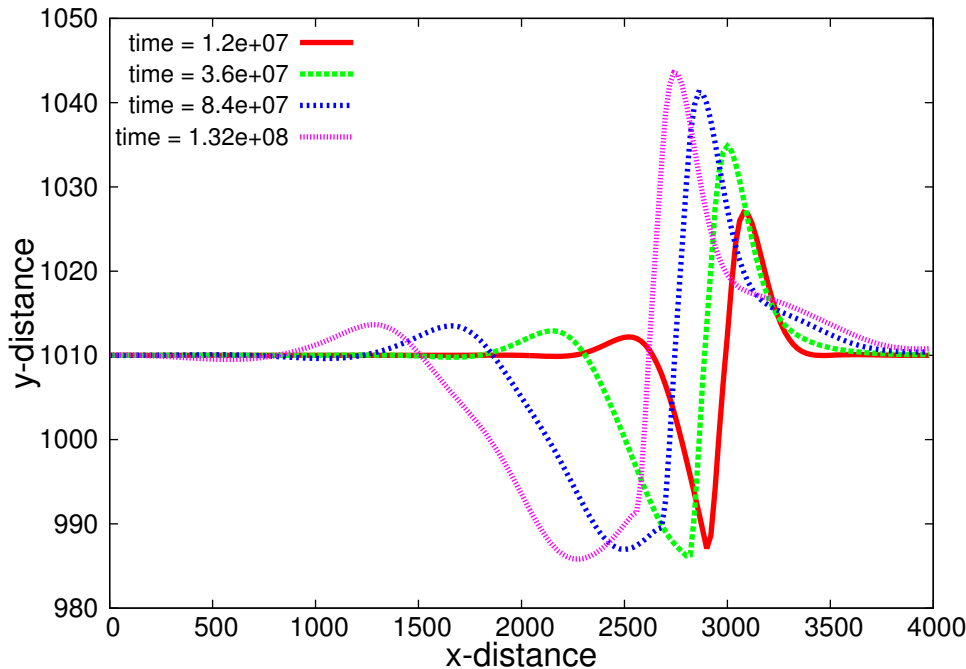


Figure 5.14: Evolution of grain boundary groove in the isotropic case for a given voltage difference = 1.5.

In the presence of electric current the groove flattens out rather than increasing in depth. While, for a given voltage difference the cathode side hillock height remains constant, the anode side hillock increases in height. For thin film interconnects this anode hillocks are related to the reliability of the device as these can grow and touch another nearby interconnect making a short circuit network.

Groove profiles for different voltage differences have been studied and compared with the thermal groove profile. It is found that the groove depth under electric current remains lesser than the thermal groove depth. The anode side hillock increases with the increase in voltage difference or electric current. On the other hand, cathode side hillock height decreases with the increase in electric current. Groove depth to anode hillock height ratios have been plotted for different potential differences, while for thermal grooving this ratio becomes close to 4.0, here with increasing electric current the ratio decreases and becomes less than 1.0 for very high currents. So, for high current densities one can observe grain boundary hillock on the anode side and large void area on the groove site, which are responsible for the failure of the interconnects.

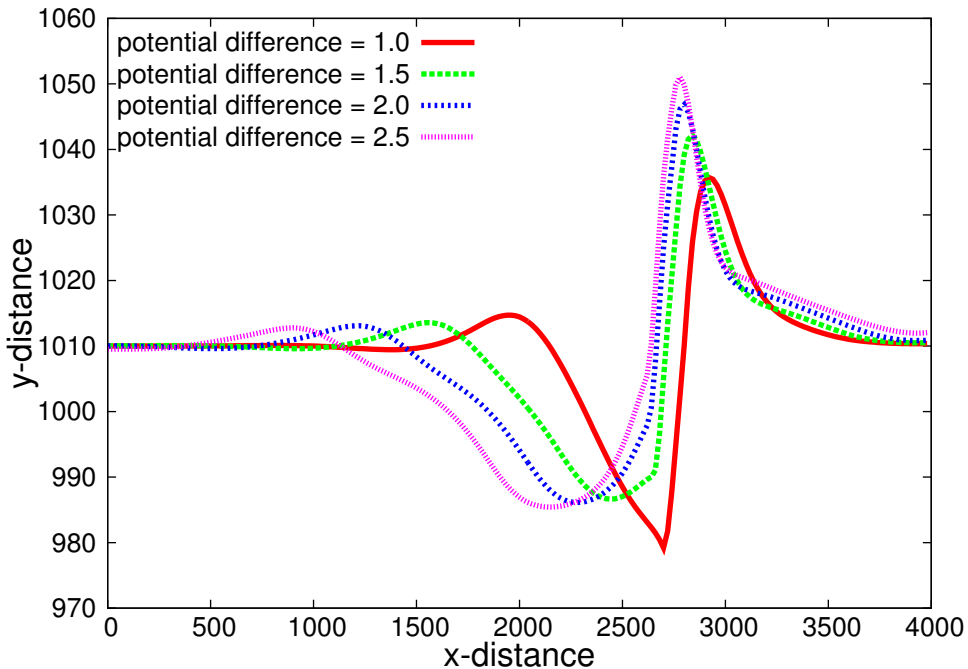


Figure 5.15: Comparison of groove profiles for different potential differences for the same timestep, where $\gamma_{gb}/\gamma_s = 1.0$ for all the cases.

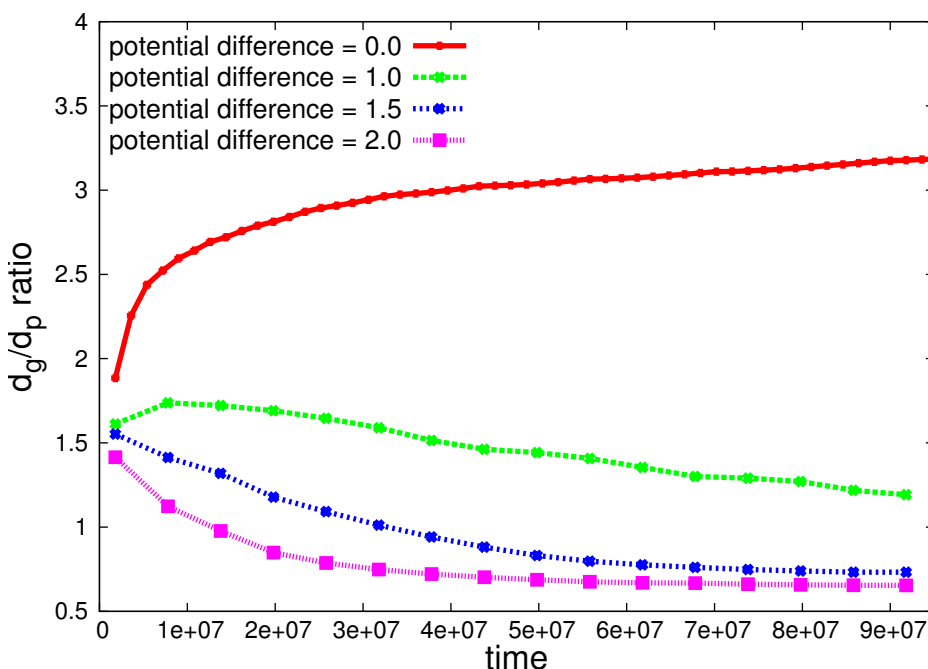
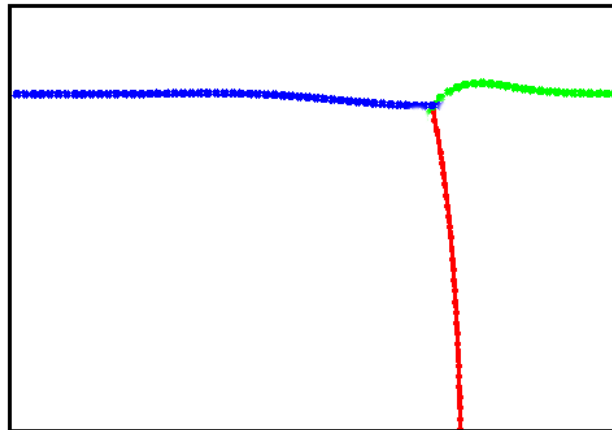
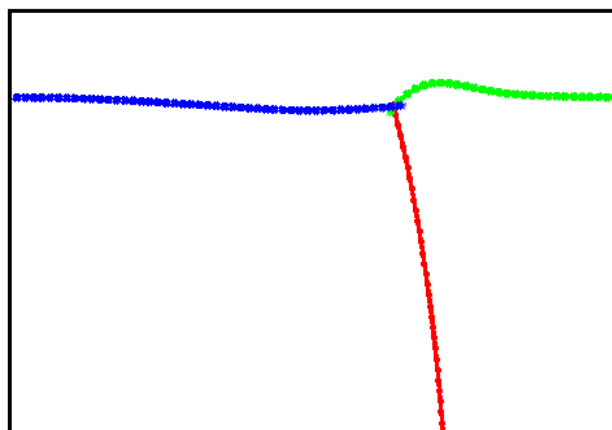


Figure 5.16: Comparison of groove depth to anode hillock height ratio for different electric potential differences, where $\gamma_{gb}/\gamma_s = 1.0$ for all the cases.

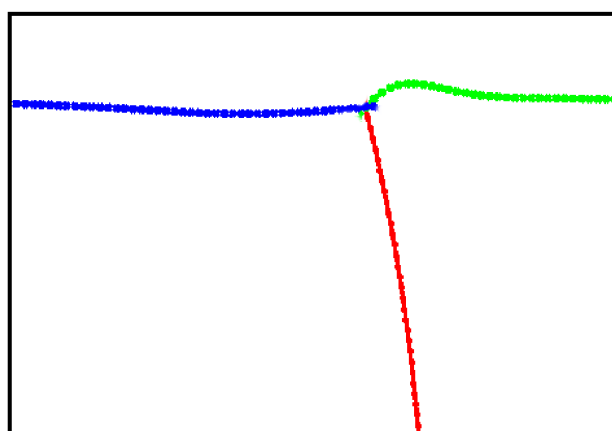
We have found another interesting phenomenon of grain boundary migration along with grain grooving due to electric currents. As discussed earlier in this chapter, this kind of grain boundary migration is related to the angle between the grain boundary and surface normal. As the angle increases from zero, surface curvature across the groove root changes significantly which imparts the driving force for boundary migration.



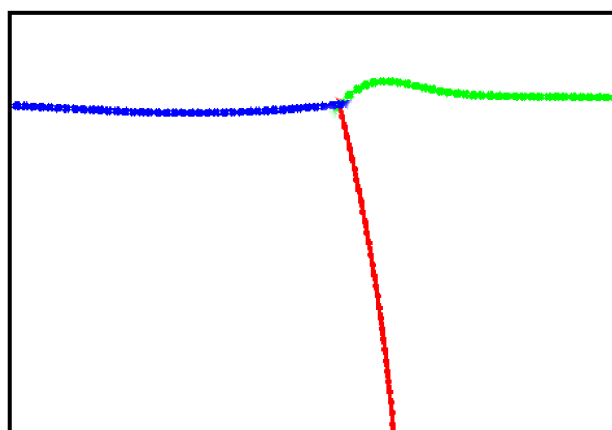
(a) time=12000000



(b) time=36000000



(c) time=60000000



(d) time=84000000

Figure 5.17: Figure showing the interfaces at different time, blue and green line representing solid-liquid interfaces and red line representing the grain boundary between two solid phases. $\gamma_{gb}/\gamma_s = 1.0$ and applied potential difference is 2.0.

Mullins[5] in his work has shown analytically that the migration velocity depends on the $\left(\frac{\theta}{\theta_c}\right)$ ratio, where θ is the angle between the grain boundary and the surface normal and θ_c is the critical angle for which a steady state migration occurs. If $\theta = 0$ then the grain boundary remains static and the groove profile sinks through the y-axis. If $0 < \theta < \theta_c$, then grain boundary migrates with a decelerating velocity and the groove profile takes a constant shape with increasing size. For $\theta = \theta_c$ grooving can not occur and the grain boundary moves indefinitely. Mullins also showed that the distance covered by the groove root(s) follows a $t^{1/4}$ dependence.

$$s = 4\lambda \left(\frac{\theta}{\theta_c}\right) (Bt)^{1/4} \quad (5.6)$$

where $4\lambda \left(\frac{\theta}{\theta_c}\right)$ term comes from the power series expansion for the solution of groove profile.

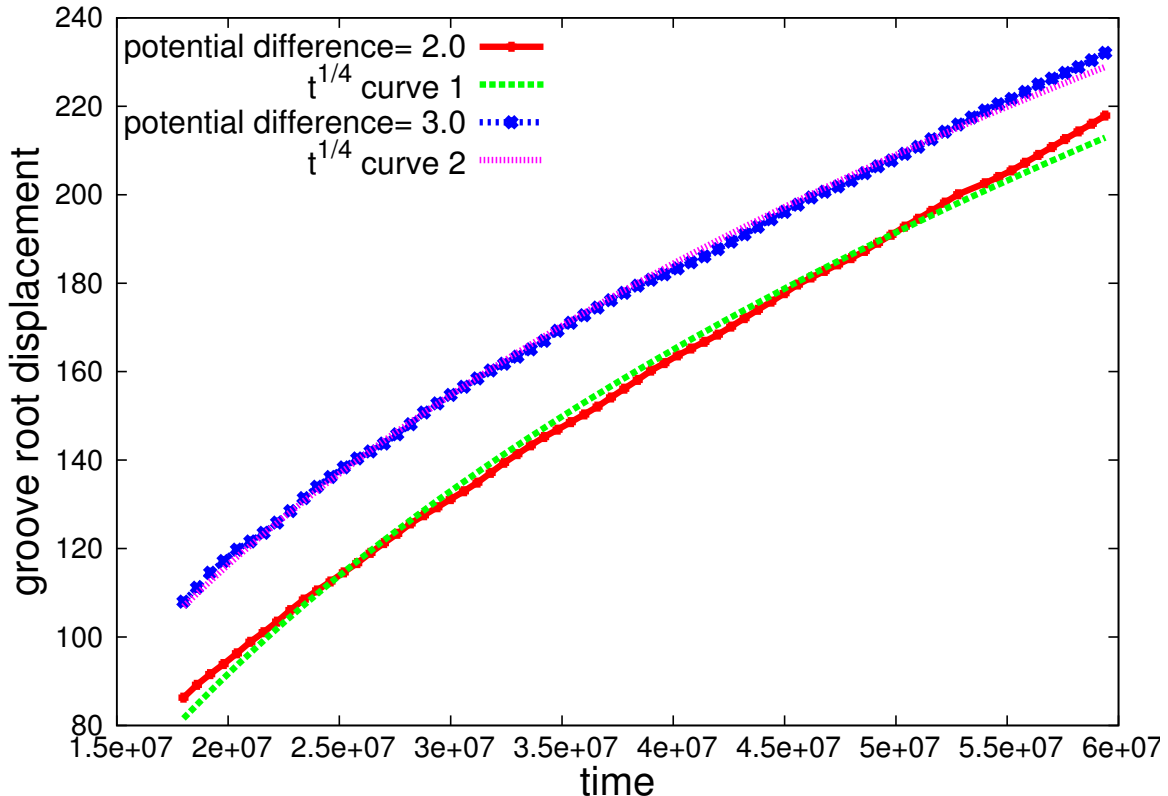


Figure 5.18: Comparison of the groove root displacement for different potential differences and fitting to $t^{1/4}$ curves; $\gamma_{gb}/\gamma_s = 1.0$ for both the cases.

Our simulations with electric current matches well with the proposed theory by Mullins. We found that groove root displacement is a function of $t^{1/4}$, which is a indication of decelerating grain boundary migration. For a given time the groove root displacement increases with increasing electric current.

We have done simulation taking the $\gamma_{gb}/\gamma_s = 0.5$ and imposing a electric potential difference of 2.0. As, γ_{gb}/γ_s ratio decreases the assumption of small slope of the groove

profile becomes more realistic. We have compared the results of isotropic case and the $\gamma_{gb}/\gamma_s = 0.5$ case and we have found a lower groove depth in the later case. As the groove surface is flatter than the isotropic case, curvature driven mass flow is lesser for the case of $\gamma_{gb}/\gamma_s = 0.5$. So, the groove can not go deep. Along with this, the electromigration force restricts the grooving phenomenon as discussed earlier.

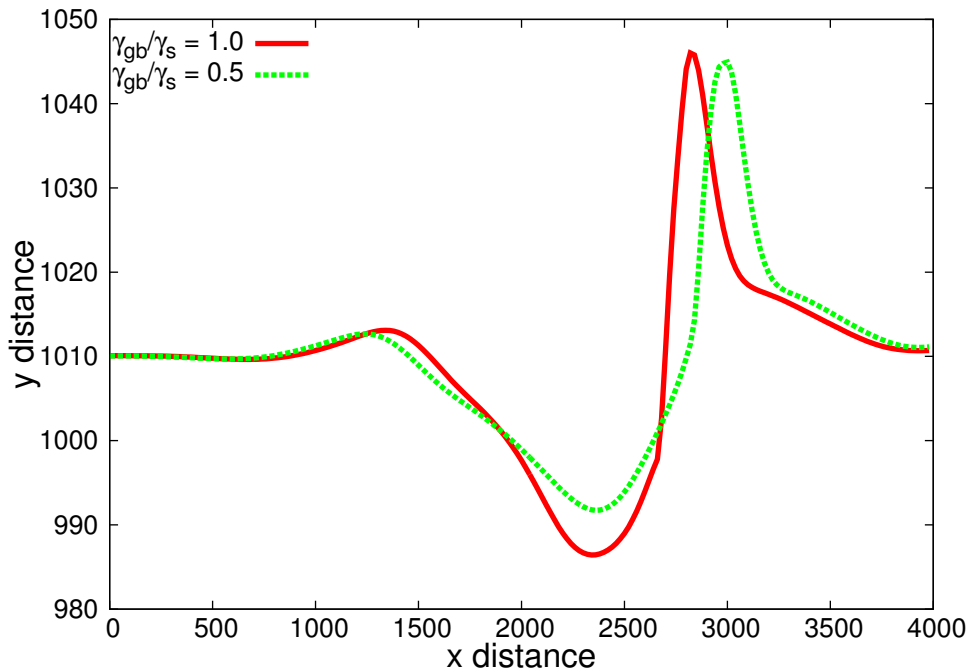


Figure 5.19: Comparison of groove profile for two different γ_{gb}/γ_s ratio under the same potential difference = 2.0.

We have also compared the groove root displacement for both the cases of γ_{gb}/γ_s . We have found that the displacement is much lower for the case of $\gamma_{gb}/\gamma_s = 0.5$, again due to the slower mass transport process. But, we observed that groove root displacement for the $\gamma_{gb}/\gamma_s = 0.5$ case follows the same $t^{1/4}$ time dependence.

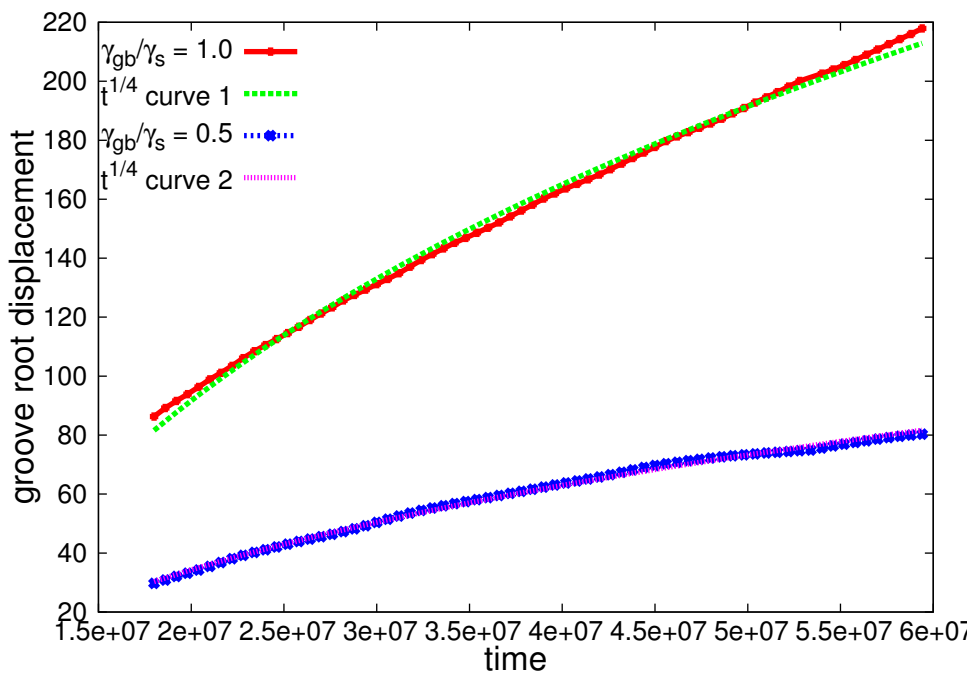


Figure 5.20: Comparison of groove profile for two different γ_{gb}/γ_s ratio under the same potential difference = 2.0.

5.3.3 3D simulation results

3D simulations have been done with the electric current taking the same model system as the earlier 3D simulations. A potential difference is applied across the x-direction. To solve the Laplace equation we have applied constant boundary condition in X-direction, no-flux in Y-direction and periodic boundary condition in Z-direction. Again, pit formation has been observed at the grain boundary vertices. Ridge formation due to electric current near the grain boundary groove can be easily observed in 3D simulation.

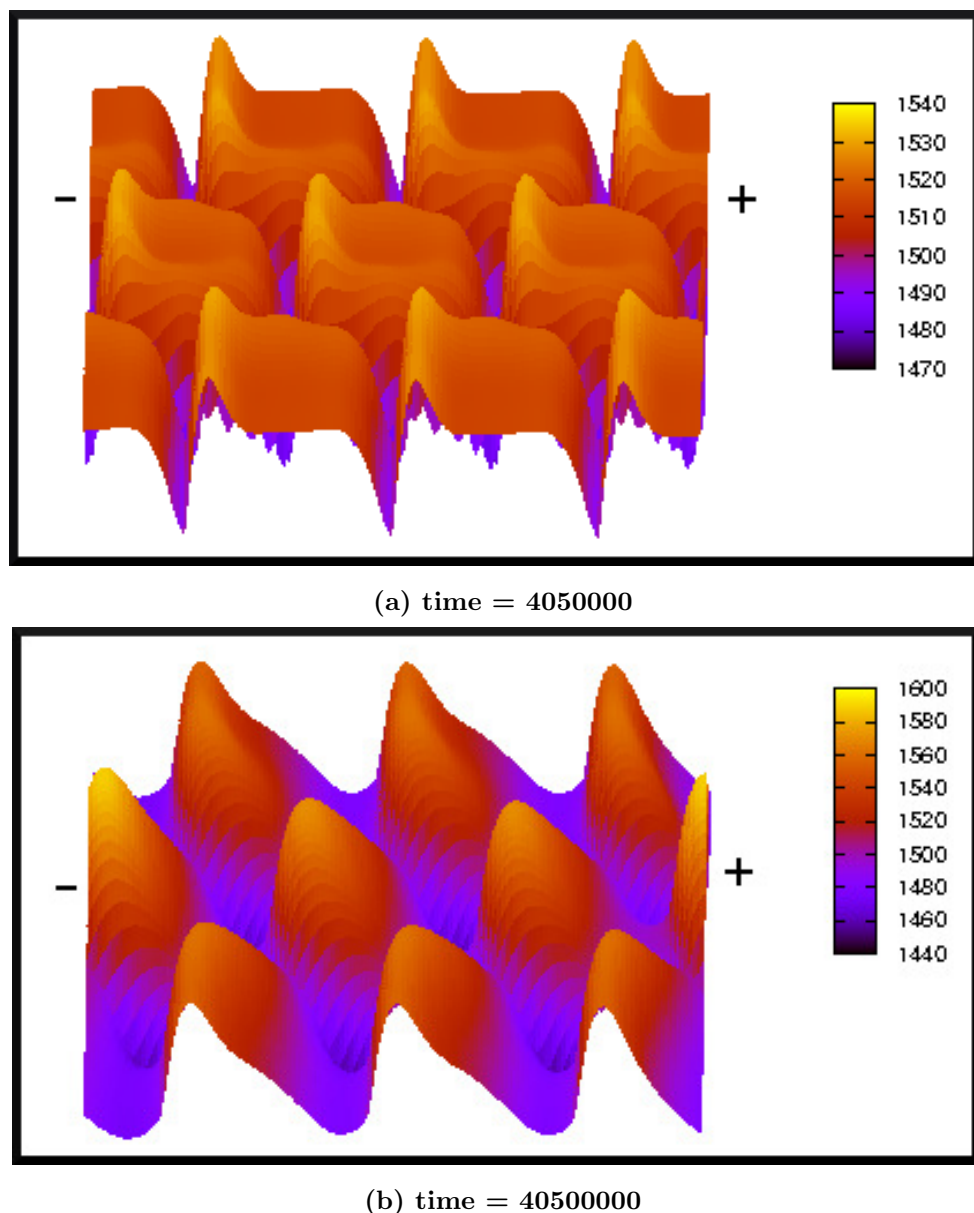


Figure 5.21: Surface plot (x-z plane) for two different time for an applied potential difference of 1.0: observation of (i) anode side hillock formation, (ii) ridge formation near grain boundary groove, (iii) pit formation at the grain boundary vertices and (iv) grain boundary migration towards cathode.

We have measured the pit depth (d_p) under the effect of electric current and compared it with the result obtained for thermal grooving. It is found that in the presence of electric current pit depth remains lower than pit depth in thermal grooving. Furthermore, the pit depth saturates in the presence of electric current. So, the chances

of hole formation are less in the presence of electric current.

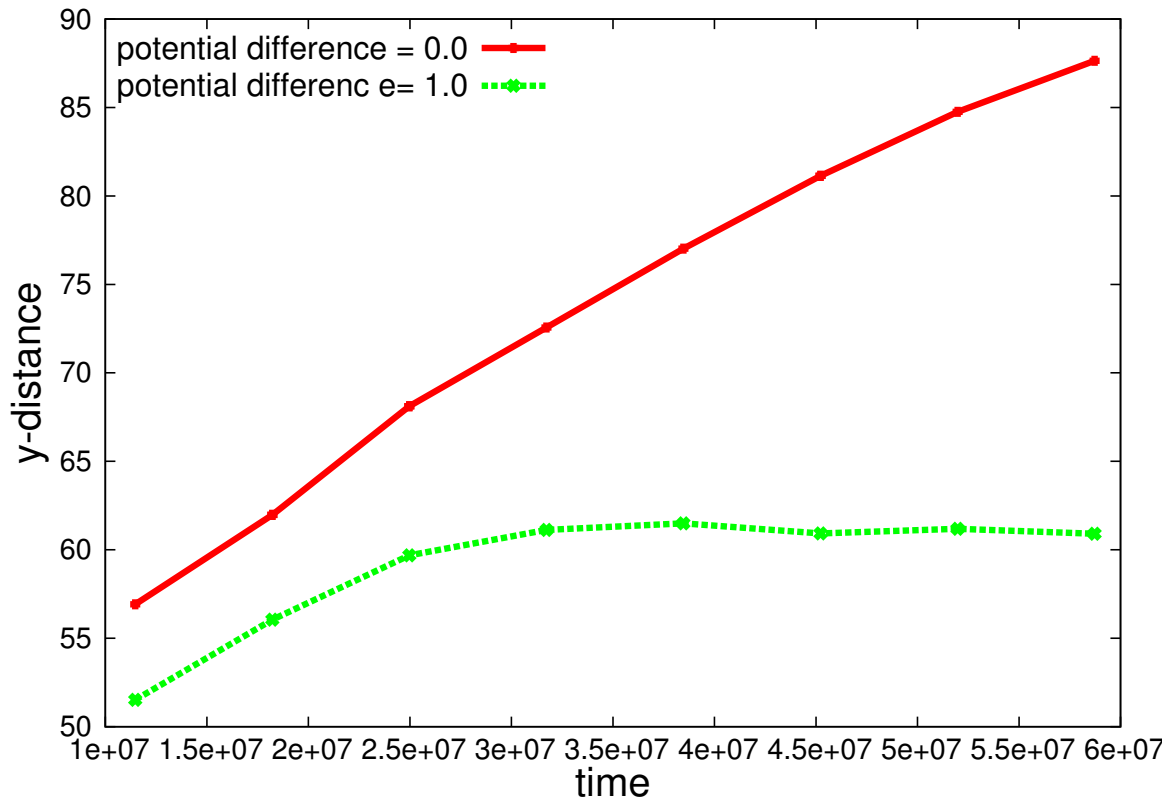


Figure 5.22: Comparison of pit depth for two different condition.

Mass Transport Under Electric Current and Temperature Gradient

As discussed in the literature review, current crowding near the corners of a narrow interconnect gives rise to excessive joule heating at the corners, while inside the bulk conductor the joule heating is uniform. So, there exist a temperature gradient near the two sides of the interconnect and the magnitude of this gradient can easily go upto $1000^{\circ}C/m$. Due to electromigration void generation can occur at the cathode side and because of that resistance increases to a high value which gives rise to excessive joule heating at cathode. The interlayer between the metal interconnect and substrate has high resistivity, during passing of current joule heating can occur at that place. So, from the above discussion it can be easily understood that there always exist a temperature gradient in the thin film interconnects due to current stressing and separating the effects of electric current and temperature gradient on mass transport is difficult. Recently, Somaiah et.al.[10] reported their experimental study of coupled electromigration and thermomigration in thin film interconnects. They observed a forward mass transport from cathode side as well as a backward mass transport from anode side. They predicted that because of excessive joule heating at the corners a temperature gradient exist from both the cathode and anode side. This experimental result motivated us to model the coupled effect of electromigration and thermomigration on the void evolution in thin film interconnects.

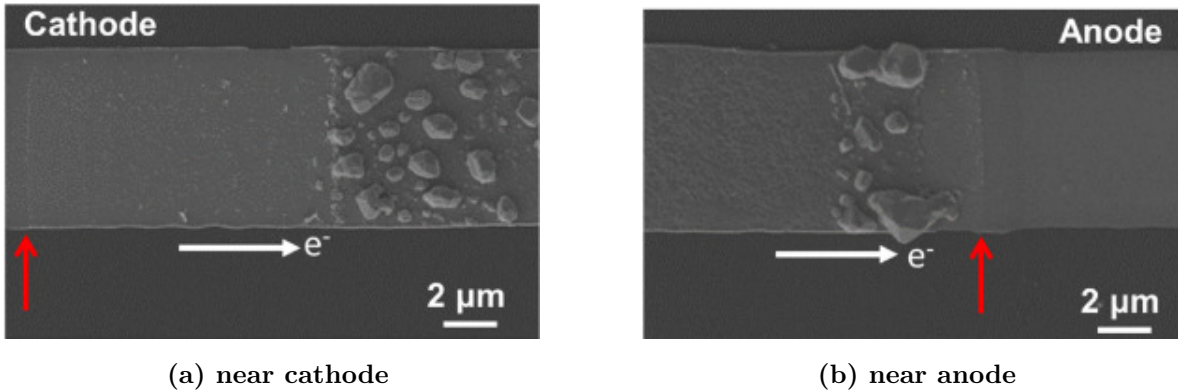


Figure 6.1: SEM images of thin film after electromigration test (a) forward mass transport on cathode side, (b) anomalous backward mass transport on anode side; red arrows show the initial positions for cathode and anode[10].

This chapter starts with the study of effect of electric current and temperature gradient individually on the grain boundary grooving and void migration for a two grain model system. Then, we have performed our simulations taking a polycrystalline solid phase and a void phase. The individual as well as coupled effect of electric current and temperature gradient have been studied thoroughly.

6.1 Mass transport through a grain boundary

A model system of two grains with the grain boundary lying parallel to the applied electric current and temperature field has been taken to understand the effect of electric current and temperature gradient on mass transport. The solid phase is surrounded by the void phase from both side. Electric current is passed from right to left, where we have imposed temperature gradient from both the side. As of now, for simplicity we have imposed only uni-directional temperature gradient along the X-direction.

6.1.1 Effect of electric current

Where the grain boundary meets the solid-void interface it starts to form groove. The electromigration wind force acts from cathode to anode direction, so the atoms tend to migrate from cathode to anode side through the grain boundary. But, for grain boundary to groove the atoms should migrate out of the grain boundary. As a result, the electromigration wind force opposes the curvature driven mass transport in the cathode side, so, the grooving can not occur properly on the cathode side. On the other hand electromigration wind force helps the curvature driven mass transport on the anode side, which is the reason for deep grooving of the interface on the anode

side. Therefore, if the electric current is high enough to overcome the curvature driven flow on the cathode side, then a unidirectional mass transport occurs from cathode to anode side and the interfaces move towards the anode side.

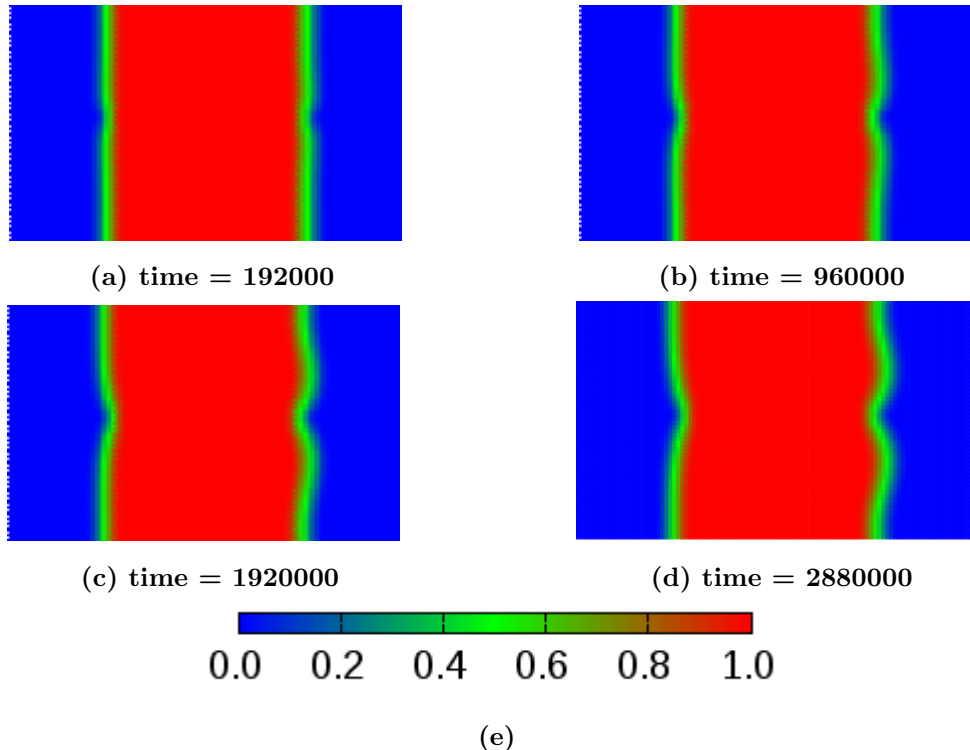


Figure 6.2: Mass transport through a grain boundary parallel to the applied electric current.

6.1.2 Effect of temperature gradient

In the presence of temperature gradient atoms start to migrate, but atoms to cover an observable distance the temperature gradient need to be very high in magnitude, that is why we do not observe thermomigration readily in our daily life. But, in the semiconductor industry especially in the solder joints thermomigration related mass transport can be easily observed. While not so much work has been done related to thermomigration in the interconnects, but it exists there because of the excessive joule heating. Unlike solid state electromigration, in the case of thermomigration the direction of atom transport depends on the element itself. Sign of the factor Q^* depends on the element, for example copper atoms have positive value Q^* , so it moves from hot to cold junction under the temperature gradient. We tried to simulate the two-grain system with a simple one dimensional temperature profile to observe the mass transport behaviour. Fig.[6.3] shows the applied temperature profile which has maximum temperature at the solid-void interface and gradually comes down to a constant value in the bulk of the solid.

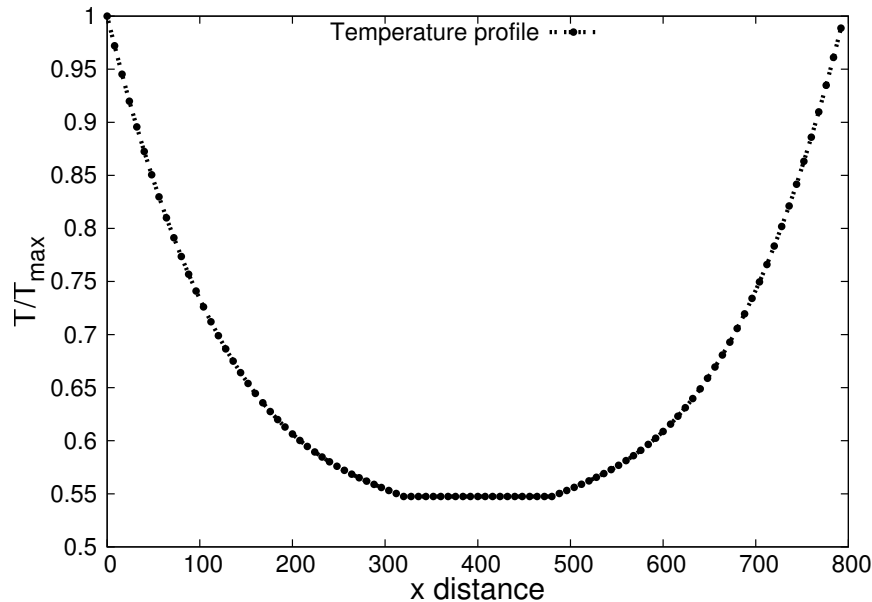


Figure 6.3: Applied temperature profile along the x-axis.

We have taken Q^* positive in our simulation, so atoms want to move from solid-void interface to inside the bulk solid. While for grain boundary groove to form atom should go out from the grain boundary. So, for the case of thermomigration from both the end groove profile can not establish properly in the both side.

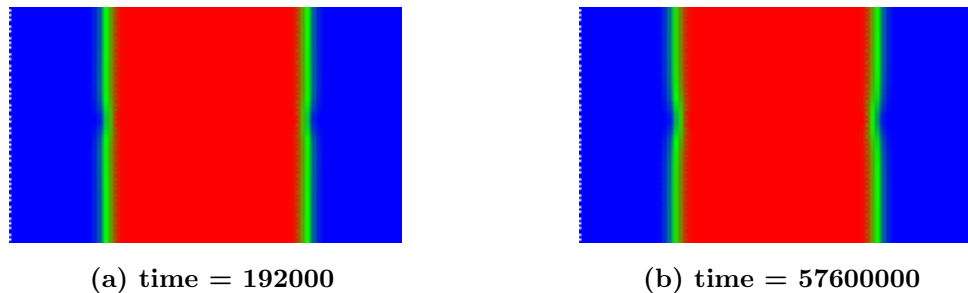
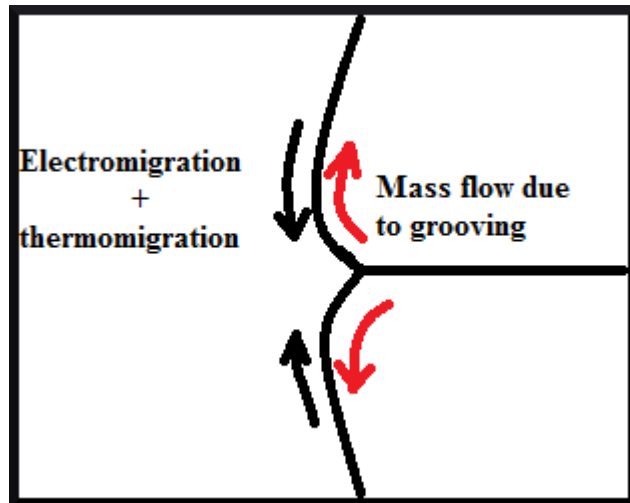


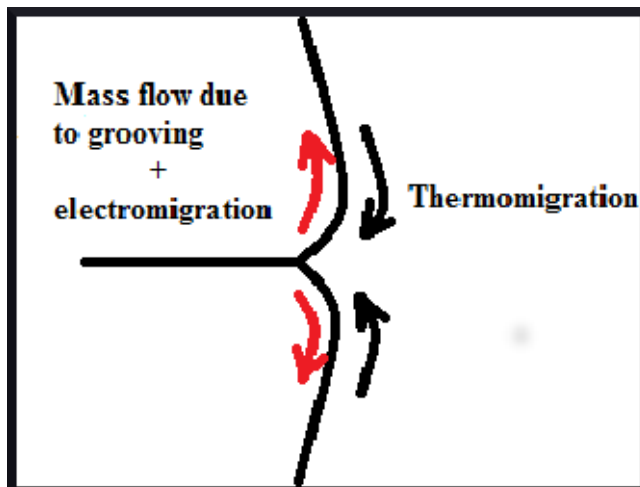
Figure 6.4: Mass transport under the temperature gradient.

6.1.3 Combined effect of electric current and temperature gradient

From the discussions in the preceding section it is easily understood that electric current and temperature gradient both act together in the cathode side and both oppose each other in the anode side. A simple schematic can explain the grooving tendency and mass transport under the effect of electric current and temperature gradient.



(a) Cathode side mass transport



(b) Anode side mass transport

Figure 6.5: Schematics to understand the mass transport processes.

The interface dynamics will depend on the interplay between the electromigration and thermomigration driving forces. When the electromigration driving force overcomes thermomigration driving force the solid-void interface will move towards anode, but when the thermomigration driving force is higher than electromigration driving force the interface does not move. We define two terms to represent the electric current and temperature effect on mass transport : (i) gradient in electric potential = $\nabla V = \frac{\Delta V}{\Delta x}$ and (ii) gradient in temperature = $\nabla T = \frac{\Delta T}{\Delta x}$, where ΔV = maximum electric potential - minimum electric potential, ΔT = maximum temperature - minimum temperature and Δx = the x-distance from the edge of the solid upto where the gradient exist.

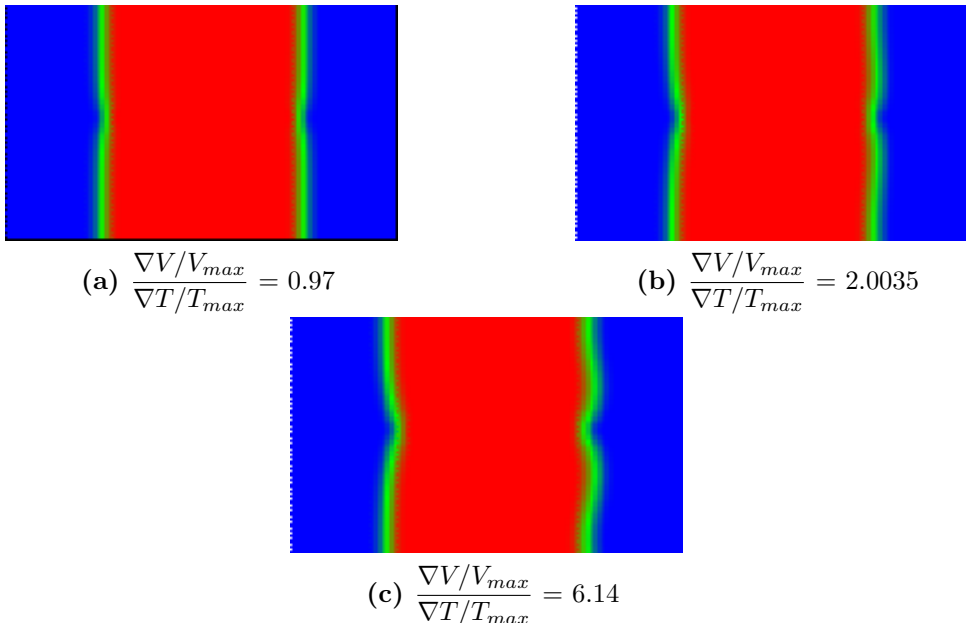


Figure 6.6: Mass transport under different combinations of electric potential gradient and temperature gradient for time = 3840000.

6.2 Mass transport in a polycrystalline solid

In a polycrystalline solid random grain boundary networks make the mass transport easier, so in contrast to the two grain problem we expect much faster interface migration. We have taken a model system consisting a void phase and a solid phase in which grains are randomly arranged. We have tried to reproduce the results found in experiments. Apart from the effect of electric current and temperature gradient, we have also found that the grain size and grain boundary network plays an important role in the mass transport, thus in the void migration. We have started our simulation with a specific microstructure and then applied electric current and temperature gradient on it.

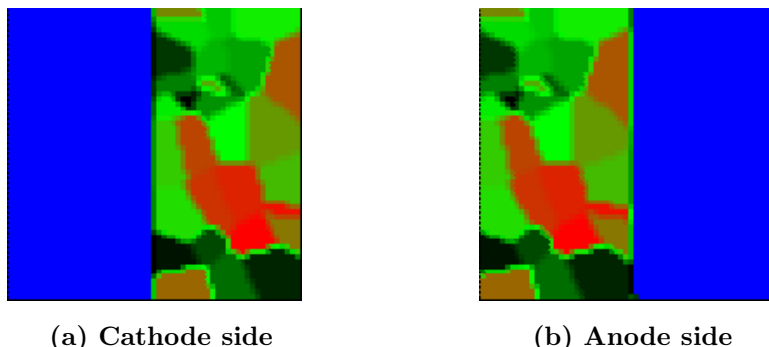


Figure 6.7: Initial system consisting a void phase (blue) and a polycrystalline solid phase.

6.2.1 Simulation results for cathode side

We have started our simulation with applying a 1D temperature field which has a decreasing value of temperature inside the solid phase. Mass flow has been observed away from the cathode side resulting the void phase to grow inside the solid phase.

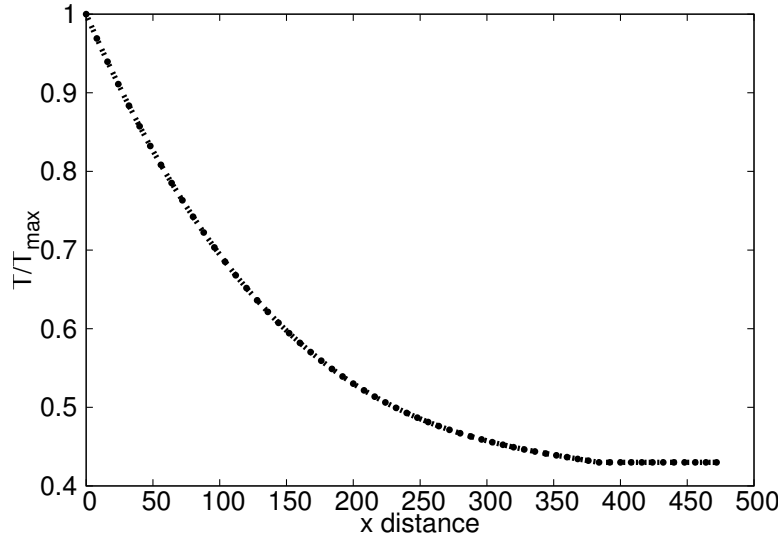


Figure 6.8: Applied temperature profile.

Here the mass transport route is the grain boundary network. The composition profile has some darker spots where the composition is higher than the bulk solid. It is concluded that these are the places where hillock forms. Grain boundary triple points are the flux divergence sites, where the flux divergence is negative, atoms get deposited there.

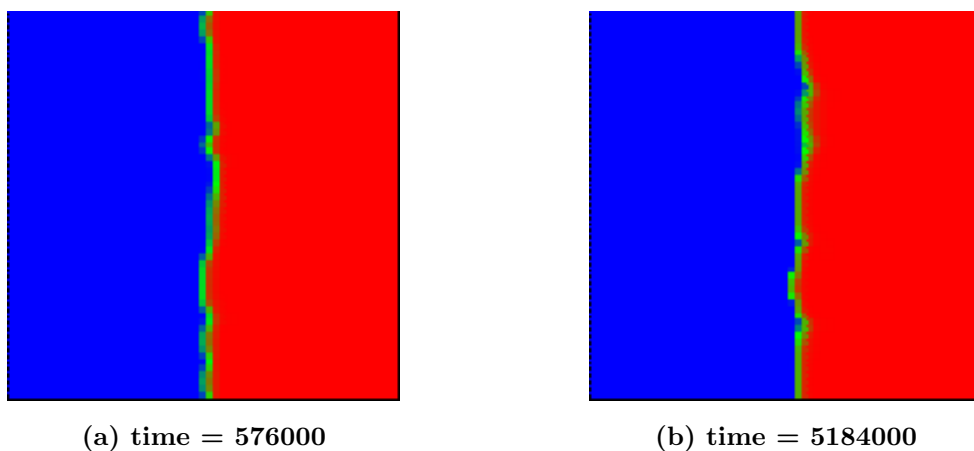


Figure 6.9: Void phase growth inside the solid phase due to temperature gradient.

Later, we have applied the electric current and observed the coupled effect of electromigration and thermomigration in a polycrystalline solid. Electric current accelerates the mass transport from cathode to anode side, so, we can observe a faster void growth in the solid phase due to coupled electromigration and thermomigration.

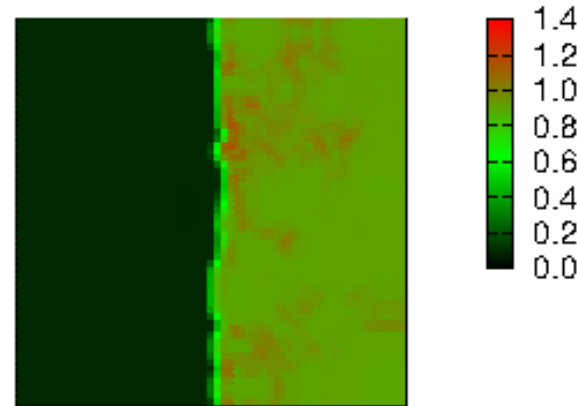


Figure 6.10: Composition profile due to temperature gradient at time = 576000, red dots showing hillocks.

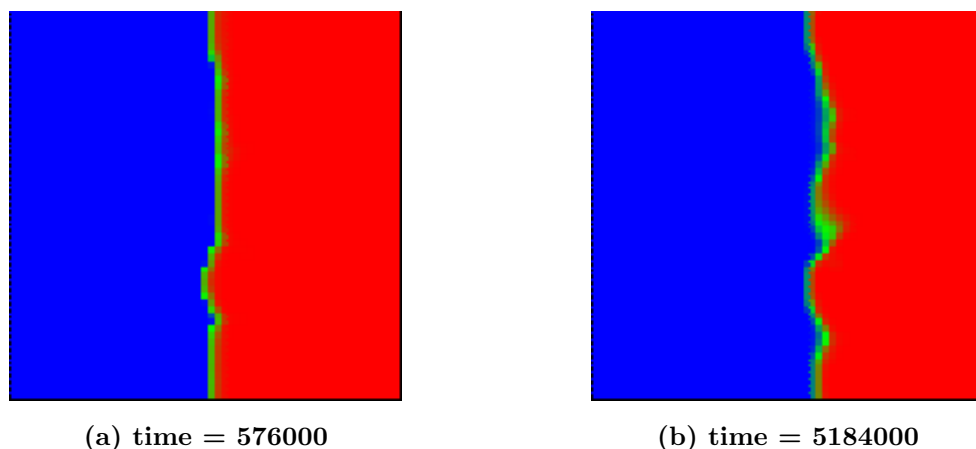


Figure 6.11: Void phase growth inside the solid phase due to coupled electric current and temperature gradient, electric potential difference = 0.5.

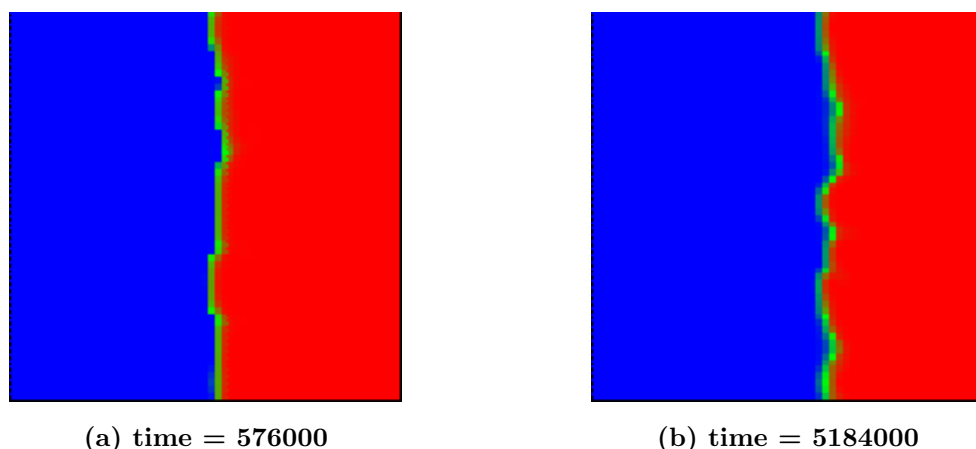


Figure 6.12: Void phase growth inside the solid phase due to coupled electric current and temperature gradient, electric potential difference = 1.0.

6.2.2 Simulation results for anode side

Again, we have started our simulation with applying a temperature gradient but for this time the gradient is in opposite direction. The maximum temperature is on the anode edge while temperature decreases to a constant value inside the solid phase. The opposite temperature profile is imparted to simulate the anomalous mass transport from anode to cathode side due to joule heating at the anode side.

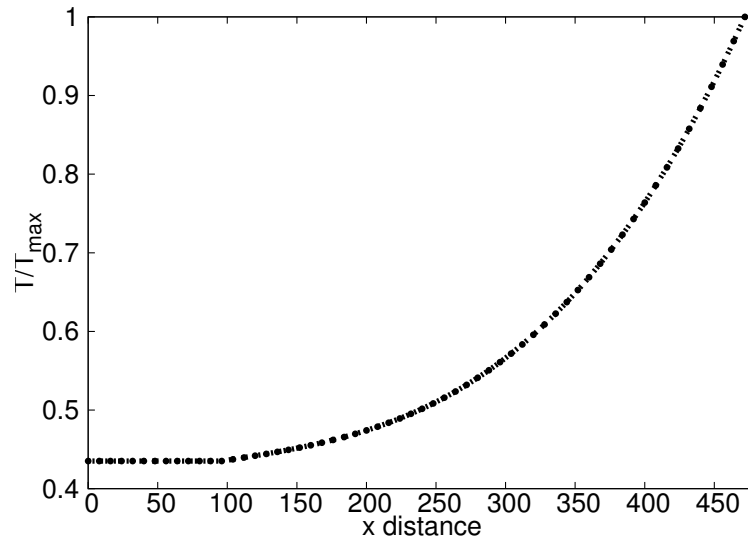


Figure 6.13: Applied temperature profile.

Simulation has been done with temperature gradient only and a backward flow of atoms towards the cathode side has been observed. Therefore, the void phase grows inside the solid phase from the anode side. Again, the grain boundary network is the route for mass transport. From the composition profile we can easily observe the hillock formation inside the solid phase.

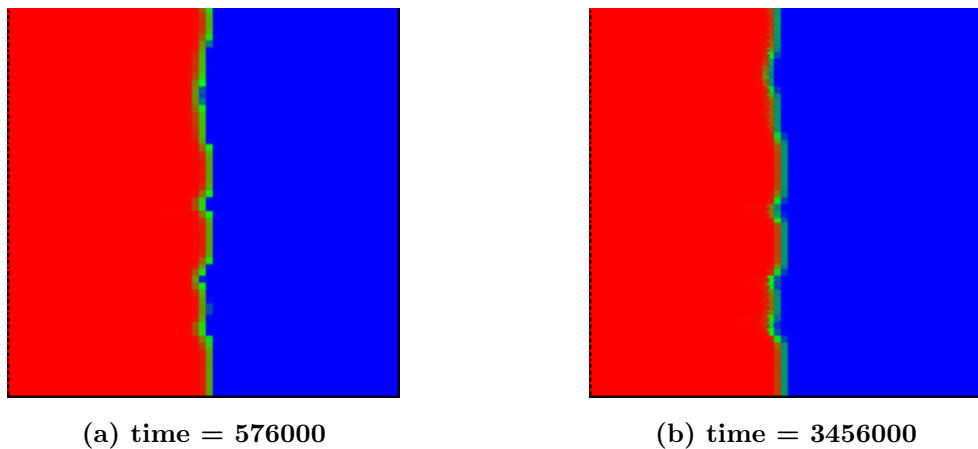


Figure 6.14: Void phase growth inside the solid phase in the presence of temperature gradient.

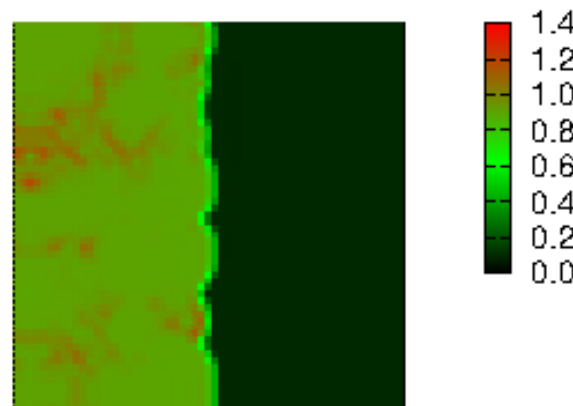


Figure 6.15: Composition profile due to temperature gradient at time = 576000, red dots showing hillocks.

Later, we have added electric current flowing from anode to cathode direction

and observed that the backward mass flow due to temperature gradient is decreasing with increasing electric current. It can be inferred that the electromigration force is opposing the thermomigration force in the anode side. When the electromigration force is small compared to the thermomigration force, the backward mass flow is still continues, Which is the case of anomalous mass transport in the anode side for the interconnects. But, if the electromigration force is higher than thermomigration force then no backward mass flow would be observed.

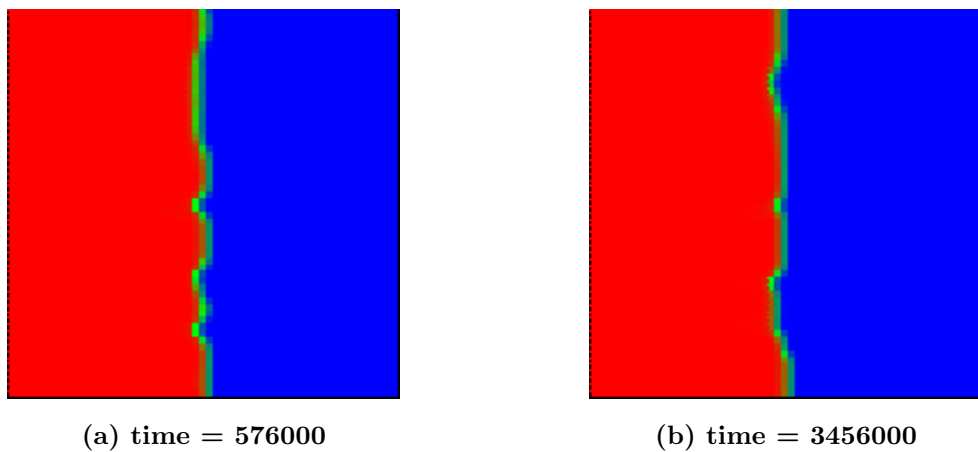


Figure 6.16: Void phase growth inside the solid phase due to coupled electric current and temperature gradient, electric potential difference = 0.1.

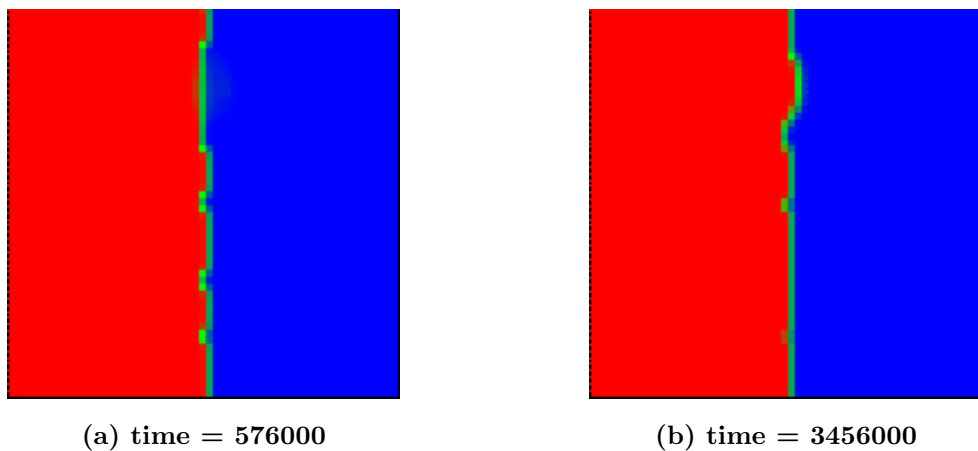
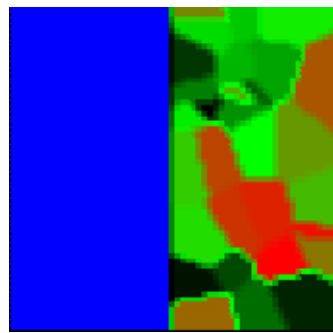


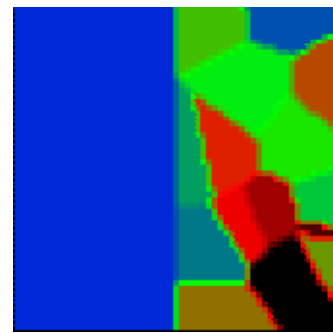
Figure 6.17: No growth of void phase is observed, electric potential difference = 0.5.

6.2.3 Effect of grain size

In order to explain the effect of grain size and thus the grain boundary network we have taken another model system in which the polycrystalline phase has half the number of grains of the earlier simulations. We have simulated the cathode side and applied the same temperature gradient and electric current in the system. We have compared the results with the earlier simulation results and found that void grows slower in the case of system with bigger grains.

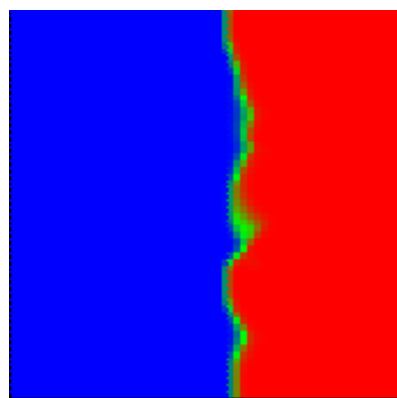


(a) Smaller grain size

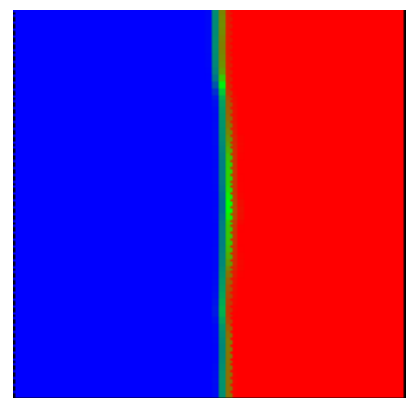


(b) bigger grain size

Figure 6.18: Comparison between the two solid phase grain structure.



(a) time = 5184000



(b) time = 5184000

Figure 6.19: Comparative study of the effect of grain size on void growth, electric potential difference = 0.5.

Summary and Conclusion

We have developed a novel phase field model using grand potential formulation to study the effect of electric current on void evolution, different surface related phenomenon such as grain boundary grooving, grain boundary pit formation at triple points, grain boundary hillock formation etc. Although these are very general physical phenomena our main focus was on the thin film interconnects in electronic devices. We have explored different reliability issues related to interconnects. Our model has sufficiently captured the underlying physics behind different kind of failure mechanisms in the interconnects. As interconnects have very small cross sectional area the current density becomes very high inside the conductor. Electrons start to interact with diffusing ions and transfer their momentum to the ions. Due to this ions tend to move in a particular direction, from cathode to anode, creating a void at the cathode side. These voids then move toward the cathode side due to accelerated atom migration around the free surface of a void. We started our work studying the void morphological changes and void dynamics inside the interconnects. Then we have imposed anisotropy in the surface energy and diffusivity separately to get various morphological changes in the void. Next, we have explored surface related problems in the interconnects. Grain boundary grooving and hillock formation have been studied in 2D simulations. In 3D simulations we have measured the pit depth for various electric currents and matched our results with analytical theory available. We have found grain boundary migration due to passing of electric current. The dynamics of grain boundary migration has been studied in the light of Mullins theory for grain boundary grooving and migration. Lastly, we have studied mass transport through grain boundaries. In this regard, we have studied the effects of electric current and temperature gradient which is coming in the picture due to the excessive joule heating at the interconnect corners. We have studied the coupled effect of electric current and temperature gradient on the void evolution at the cathode and anode side. We are now going to discuss all the major findings of our research.

- 1) We have defined a parameter χ which represents the interplay between the surface energy contribution and the electric current. We have found that with the increasing value of χ voids migrate faster toward the cathode and the increase in volume is also higher. We inferred that with increasing χ electromigration force dominates over the surface energy contribution. So, the atoms move at a fast rate through the surface of the void and the void volume increases.
- 2) The void volume changes linearly for all the χ values in our simulation regime. We can correlate the void volume increase with the resistance increase in the circuit. Experimental results show that circuit resistance increases linearly with time and suddenly it becomes extremely high value. Extremely high resistance indicate the circuit break.
- 3) The shape of the void elongates when exposed to high electric current. When an atom is removed from the top surface of the void, a gradient in diffusion potential exists because of which atoms get transported from the cathode side to the top of the void. The gradient in diffusion potential depends on electric current passing through the line. If current is very high then atoms will be transported very fast from the cathode side which gives rise to an instability on the cathode side. So, to keep the gradient in diffusion potential lower the void elongates in the cathode side.
- 4) After implementing the surface energy anisotropy the void morphology resembles the wulff shape. With increasing the value of χ it takes an elongated wulff shape.
- 5) With the diffusivity anisotropy the void shape takes a distorted four fold faceted shape. The distortion is because of the atomic flux from the cathode to anode side. The reason behind the faceted void is that the surface wants to retain those planes where the diffusivity is lowest, as the lowest diffusion rate will actually determine the rate of mass transport.
- 6) We have used the multi-phase field model to simulate the grain boundary grooving at the grain boundary and free surface junction. We have benchmarked our model with the analytical solution available. We have done 3D simulations and observed pit formation at the triple junctions. The measured pit depth has also been matched with analytical solution available for pit formation.
- 7) We have imparted the electric current into our grooving system and found an unsymmetrical grooving across the groove root for all the cases of applied electric current. The cathode side of groove surface forms ridge like shape, on the other hand anode side forms a steep hillock. With time the anode side hillock height increases as a function

of $t^{1/4}$ and the cathode side fattens out.

- 8) The anode side hillock height is much higher than the hillock height for thermal grooving. These kind of grain boundary hillocks have been found in experiments and can become a potential threat to the reliability of interconnects as these can grow and touch some other nearby interconnect, making a short circuit.
- 9) After sometime, the groove depth becomes sluggish and the groove profile takes a constant shape but increase in size with time. As the electron wind force is very high, a high rate of mass flow occurs from the cathode to anode side. This flow makes the surface on cathode side of the groove much flatter. As the surface curvature decreases on the cathode side grooving becomes sluggish.
- 10) We have observed grain boundary migration in the presence of electric current. The groove root angle wants to retain the equilibrium angle but there is a high mass flow from the cathode side which makes the groove surface flatter, so, the groove root rotates inside and retain the equilibrium angle. due to this rotation the grain boundary which is attached to the groove root also bows inside. Due to this the grain boundary makes a certain angle with the free surface normal. The surface curvature difference across the groove root along with the grain boundary curvature drives the grain boundary-groove system to migrate. Though the contribution from grain boundary curvature is very less compared to the surface curvature difference.
- 11) The distance covered by the groove root is found to be a function of $t^{1/4}$ which is also predicted by Mullins for a decelerating grain boundary-groove system. From this we can infer that the angle made by the grain boundary with the surface normal is below the critical angle θ_c for which grain boundary moves indefinitely.
- 12) We have compared the groove profiles for two different γ_{gb}/γ_s ratios. We found that groove depth decreases for the lower value of γ_{gb}/γ_s . With decrease in the ratio of γ_{gb}/γ_s groove profile becomes much flatter with lower curvature along the groove surface. So, curvature driven mass flow becomes less with decreasing value of γ_{gb}/γ_s ratio. Groove can not penetrate deeper due to lesser driving force. Along with this the electric current effect makes the groove surface more flatter. So, the groove penetrates less for the case of lower γ_{gb}/γ_s ratio.
- 13) We have measured the pit depth from the results of 3D simulation in the presence of electric current. We have compared the result with the pit depth measured during thermal grooving and found that the pit depth remains small in the presence of electric current. In the case of electric current, pit depth saturates to a equilibrium value and

after that it does not increase. So, pit formation is not an important issue of concern for the case of electric current. While for thermal grooving continuously growing pit can separate the grains and produce islands of grains.

14) In the thin film interconnects temperature can rise to a very high value due to excessive joule heating at some places. At the corners and bends temperature goes up because of current crowding. So, in general temperature profile is not uniform throughout the interconnect, very high temperature gradient may exist along the interconnect. We know that if the temperature gradient reaches as high as $1000^{\circ}\text{C}/\text{m}$ then atoms start to migrate. We have studied the influence of temperature gradient in the mass transport process. We have simulated the situation where temperature gradient exists at the corners of interconnect with a constant temperature inside the bulk. In this case, we have considered the mass transport through the grain boundaries. For the case of copper atoms mass transport occurs at the opposite direction of temperature gradient which means from hot to cold junction. We found that the void-solid interface moves into the solid phase from both the cathode and anode side. Mass flow occurred through the random grain boundary networks and mass accumulation occurred at the places where flux divergence became negative.

15) In the presence of electric current the situation becomes more realistic, we have found the high rate of forward mass transport from the cathode side due to coupled electric current and temperature gradient. As, electromigration wind force acts unidirectionally towards the anode, in the cathode side the two driving forces add up to produce faster mass transport towards the anode.

16) But in the anode side there are two possibilities, which one would be observed that solely depends on the magnitude of the two driving forces. If the electromigration force is higher than the thermomigration force then the atoms will move unidirectionally from cathode to anode side. On the other hand, if the thermomigration force is higher than the electromigration force then there will be a backward mass flow from anode side towards the cathode side. So, if the thermomigration force is very high then void formation occurs from both the side of interconnect. This phenomenon has been observed in the experiments[10].

17) We have also studied the grain size effect on the void migration due the coupled electro and thermomigration. It is found that with bigger size grains the migration is sluggish. The reason is that with increase in grain size the grain boundary network decreases in area, so, mass transport is hindered.

Future Works

- Study the coupled effect of electric current, temperature gradient and stress field on void evolution and morphological change.
- Study different types solid state phase transformations under the effect of electric current.

Numerical Methods

To solve the three coupled equations finite difference method has been used. To solve the 1D Laplace equation we used Thomas algorithm and for the 2D case we used Gauss-Seidel method. Both the schemes will be discussed in detail in the next section. For simulating a polycrystalline microstructure voronoi tessellation has been used. The discretization schemes for isotropic case and anisotropic case will be discussed separately.

A.1 Thomas Algorithm

In this method a tridiagonal system of equations are solved by using the simple Gaussian elimination. This is used to solve a equation in one direction. The system of equations has a form of

$$a_i x_{i-1} + b_i x_i + c_i x_{i+1} = d_i$$

$$\begin{bmatrix} b_1 & c_1 & & 0 \\ a_2 & b_2 & c_2 & \\ & a_3 & b_3 & \ddots \\ & \ddots & \ddots & c_{n-1} \\ 0 & & a_n & b_n \end{bmatrix} \times \begin{bmatrix} x_1 \\ x_2 \\ x_3 \\ \vdots \\ x_n \end{bmatrix} = \begin{bmatrix} d_1 \\ d_2 \\ d_3 \\ \vdots \\ d_n \end{bmatrix}$$

where $a_1 = 0$ and $c_n = 0$. The system of equation is solved by doing a forward sweep for modifying the coefficients and eliminating x_i 's until the the last equation is reached. For the last equation we get the value of x_n directly. Then we perform a back substitution to get x_{n-1}, x_{n-2} etc. The algorithm goes like this :

$$c'_i = \frac{c_i}{b_i} \quad \text{for } i=1$$

$$= \frac{c_i}{b_i - a_i * c'_{i-1}} \quad \text{for } i = 2, 3..n-1$$

$$b'_i = 1 \quad \text{for all } i's$$

$$d'_i = \frac{d_i}{b_i} \quad \text{for } i = 1$$

$$= \frac{d_i - a_i * d'_{i-1}}{b_i - a_i * c'_{i-1}} \quad \text{for } i = 2, 3..n$$

The solution is then obtained by back substitution:

$$x_n = d'_n$$

$$x_i = d'_i - c'_i * x_{i+1} \quad \text{for } i = n-1, n-2..1$$

A.2 Red-black Gauss-Seidel method

Gauss-Seidel method is an iterative method to solve linear equations using an initial guess value. As soon as a new approximation for an unknown is found it is used in the next step. the process of iteration is continued until the degree of tolerance is achieved. To solve the 2-D Laplace equation this method is highly effective. We can understand the algorithm by the following 5-point stencil method:

i,j+1

i-1,j i,j i+1,j

i,j-1

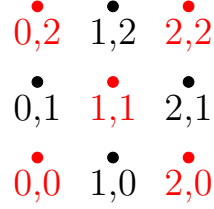
Suppose, the Laplace equation is $\nabla^2(V) = 0$ or $\frac{\partial^2 V}{\partial x^2} + \frac{\partial^2 V}{\partial y^2} = 0$.

Discretization of this equation gives the solution for $V_{i,j}$ as follows:

$$V_{i,j} = \frac{1}{4} [V_{i,j-1} + V_{i,j+1} + V_{i-1,j} + V_{i+1,j}] .$$

So, the value at each point is depended only on the surrounding four points. This property can be exploited to efficiently calculate the values at each point. Note, when $(i+j)$ is even, value at that point only depends on odd values of $(i+j)$ and vice versa. So, we can divide the whole grid into even and odd points and name them as red and

black points. First, we will solve for all the red points in one go and then we will use this updated values to calculate all the black points. This method is very useful in parallel computing.



A.3 Discretization Scheme

A.3.1 Discretization of isotropic model

Discretization for Laplacian of ϕ :

$$\nabla^2 \phi = \left[\frac{\partial^2 \phi}{\partial x^2} + \frac{\partial^2 \phi}{\partial y^2} \right]$$

$$= \left[\frac{(\phi_{i+1,j}^t - \phi_{i,j}^t)}{dx} - \frac{(\phi_{i,j}^t - \phi_{i-1,j}^t)}{dx} + \frac{(\phi_{i,j+1}^t - \phi_{i,j}^t)}{dy} - \frac{(\phi_{i,j}^t - \phi_{i,j-1}^t)}{dy} \right]$$

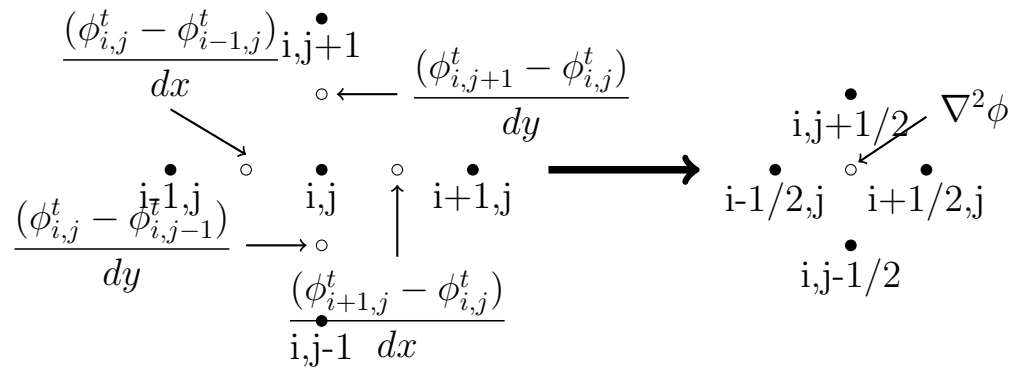


Figure A.1: Discretization of the domain for calculating $\nabla^2 \phi$

Discretization for Laplace equation:

$$\nabla \cdot (\zeta(\phi) \nabla V) = 0$$

$$\begin{aligned} & \frac{\zeta(\phi) \frac{\partial V}{\partial x}|_i - \zeta(\phi) \frac{\partial V}{\partial x}|_{i-1}}{\Delta x} + \frac{\zeta(\phi) \frac{\partial V}{\partial y}|_j - \zeta(\phi) \frac{\partial V}{\partial y}|_{j-1}}{\Delta y} = 0 \\ & \frac{(\zeta(\phi)_{i+1} + \zeta(\phi)_i) V_{i+1} - V_i}{2 \Delta x} - \frac{(\zeta(\phi)_i + \zeta(\phi)_{i-1}) V_i - V_{i-1}}{2 \Delta x} + \end{aligned}$$

$$\frac{\frac{(\zeta(\phi)_{j+1} + \zeta(\phi)_j) V_{j+1} - V_j}{\Delta y} - \frac{(\zeta(\phi)_j + \zeta(\phi)_{j-1}) V_j - V_{j-1}}{\Delta y}}{\Delta y} = 0$$

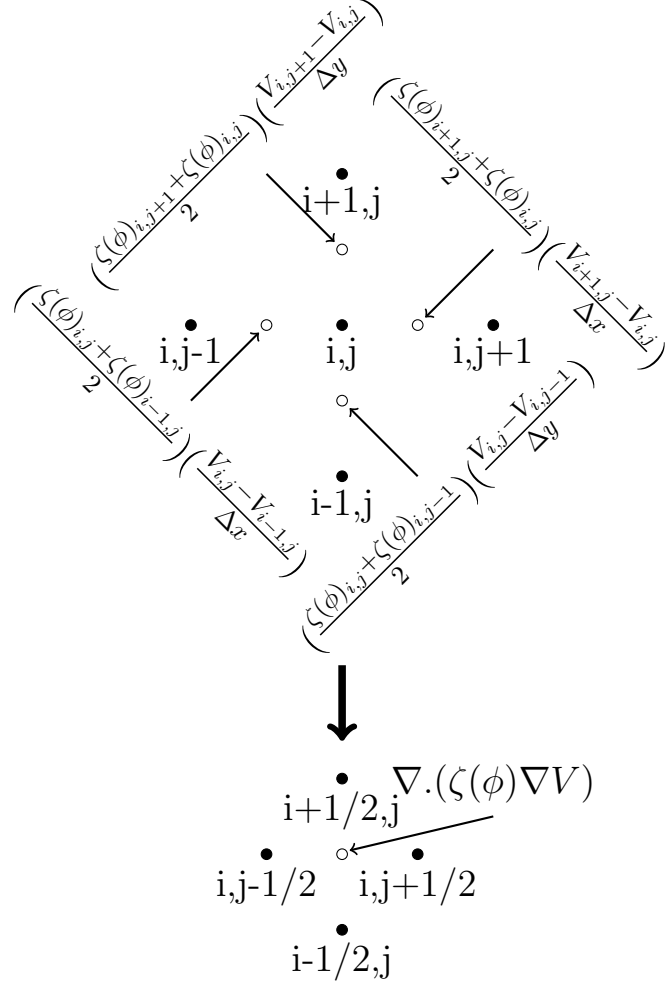


Figure A.2: Discretization of Laplace equation.

If $\Delta x = \Delta y$ then we can simplify the equation as:

$$V_{i,j} = \frac{1}{(\zeta(\phi)_{i+1} + 2\zeta(\phi)_i + \zeta(\phi)_{i-1} + \zeta(\phi)_{j+1} + 2\zeta(\phi)_j + \zeta(\phi)_{j-1})} [V_{i+1,j}(\zeta(\phi)_{i+1} + \zeta(\phi)_i) + V_{i-1,j}(\zeta(\phi)_i + \zeta(\phi)_{i-1}) + V_{i,j+1}(\zeta(\phi)_j + \zeta(\phi)_{j+1}) + V_{i,j-1}(\zeta(\phi)_j + \zeta(\phi)_{j-1})]$$

A.3.2 Discretization of anisotropic model

Anisotropic surface energy

calculation of $\frac{\partial}{\partial \phi_x} (a_c |\nabla \phi|)^2$:

$$1. \text{ calculation of } \phi_x: \phi_x = \frac{\partial \phi}{\partial x} = \frac{\phi_{i+1,j} - \phi_{i,j}}{\Delta x}$$

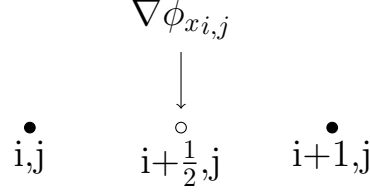


Figure A.3: Discretization of ϕ_x for $\frac{\partial}{\partial \phi_x} (a_c |\nabla \phi|)^2$.

$$2. \text{ calculation of } \phi_y : \phi_y = \frac{\partial \phi}{\partial y} = \frac{1}{4\Delta y} (\phi_{i,j+1} + \phi_{i+1,j+1} - \phi_{i,j-1} - \phi_{i+1,j-1})$$

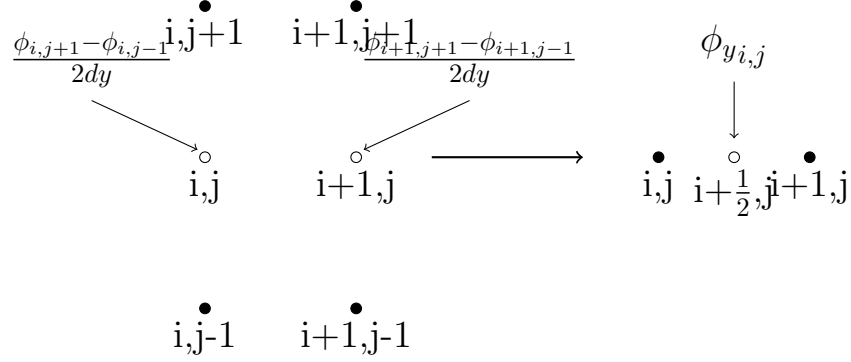


Figure A.4: Discretization of ϕ_y for $\frac{\partial}{\partial \phi_x} (a_c |\nabla \phi|)^2$.

calculation of $\frac{\partial}{\partial \phi_y} (a_c |\nabla \phi|)^2$:

$$1. \text{ calculation of } \phi_x: \phi_x = \frac{1}{4\Delta x} (\phi_{i+1,j} + \phi_{i+1,j+1} - \phi_{i-1,j} - \phi_{i-1,j+1})$$

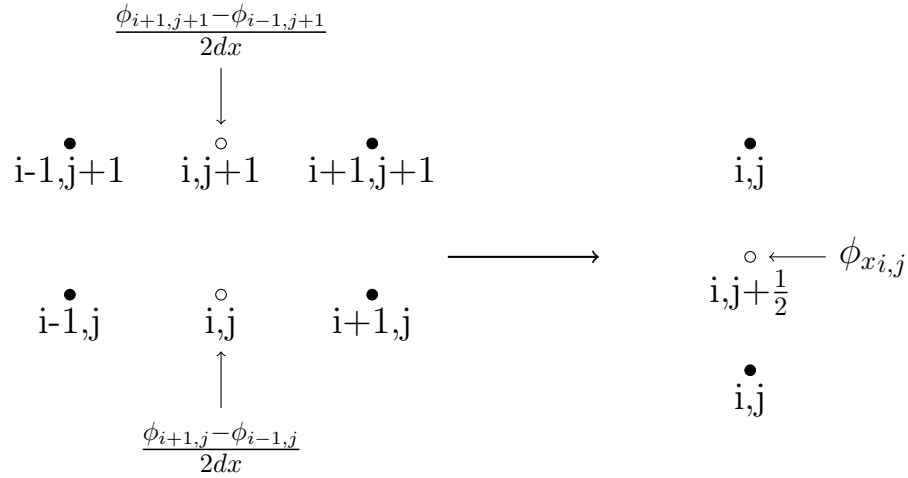


Figure A.5: Discretization of ϕ_x for $\frac{\partial}{\partial \phi_y} (a_c |\nabla \phi|)^2$.

$$2. \text{ calculation of } \phi_y: \phi_y = \frac{\phi_{i,j+1} - \phi_{i,j}}{\Delta y}$$

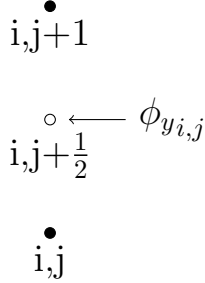


Figure A.6: Discretization of ϕ_y for $\frac{\partial}{\partial \phi_y} (a_c |\nabla \phi|)^2$.

To calculate the divergence of $\frac{\partial}{\partial \phi} (a_c |\nabla \phi|)^2$ a backward difference scheme is applied:

$$\nabla \cdot \left[\frac{\partial}{\partial \phi} (a_c |\nabla \phi|)^2 \right] = \frac{\left(\frac{\partial}{\partial \phi_x} (a_c |\nabla \phi|)^2 \right) |_{i,j} - \left(\frac{\partial}{\partial \phi_x} (a_c |\nabla \phi|)^2 \right) |_{i-1,j}}{dx} + \\ \frac{\left(\frac{\partial}{\partial \phi_y} (a_c |\nabla \phi|)^2 \right) |_{i,j} - \left(\frac{\partial}{\partial \phi_y} (a_c |\nabla \phi|)^2 \right) |_{i,j-1}}{dy}$$

Discretization for anisotropic diffusivity

Like the case for anisotropic surface energy, to calculate the D_{xx}, D_{xy}, D_{yx} and D_{yy} , ϕ_x and ϕ_y are calculated using a forward difference scheme according to the direction. Then to calculate the fluxes J_x and J_y again a forward difference scheme is applied to get all the values in between the two nodes.

$$J_x = - (D_{xx} \nabla_x \tilde{\mu} + D_{xy} \nabla_y \tilde{\mu}) \frac{\frac{\partial c}{\partial \mu}}{2\Omega}$$

$$J_y = - (D_{yx} \nabla_x \tilde{\mu} + D_{yy} \nabla_y \tilde{\mu}) \frac{\frac{\partial c}{\partial \mu}}{2\Omega}$$

$$\begin{array}{c}
 \frac{\tilde{\mu}_{i+1,j+1} - \tilde{\mu}_{i-1,j+1}}{2\Delta y} \nabla_y \tilde{\mu}_{i,j} \\
 \swarrow \quad \searrow \\
 \bullet_{i,j} \quad \circ_{i+\frac{1}{2},j+1} \quad \bullet_{i+1,j}
 \end{array}
 \qquad
 \begin{array}{c}
 \frac{\tilde{\mu}_{i+1,j} - \tilde{\mu}_{i-1,j}}{2\Delta y} \\
 \swarrow \quad \searrow \\
 \bullet_{i,j-1} \quad \bullet_{i+1,j-1}
 \end{array}$$

Figure A.7: Discretization of $\nabla_x \tilde{\mu}$ and $\nabla_y \tilde{\mu}$ for J_x

$$\begin{array}{c}
 \frac{\tilde{\mu}_{i+1,j+1} - \tilde{\mu}_{i-1,j+1}}{2\Delta x} \\
 \downarrow \\
 \bullet_{i-1,j+1} \quad \bullet_{i,j+1} \quad \bullet_{i+1,j+1} \\
 \circ_{i,j+\frac{1}{2}} \longleftarrow \nabla_x \tilde{\mu}_{i,j} \\
 \bullet_{i-1,j} \quad \bullet_{i,j} \quad \bullet_{i+1,j} \\
 \frac{\tilde{\mu}_{i+1,j} - \tilde{\mu}_{i-1,j}}{2\Delta x} \\
 \qquad \qquad \qquad \bullet_{i,j+\frac{1}{2}} \longleftarrow \nabla_y \tilde{\mu}_{i,j} \\
 \qquad \qquad \qquad \bullet_{i,j}
 \end{array}$$

Figure A.8: Discretization of $\nabla_x \tilde{\mu}$ and $\nabla_y \tilde{\mu}$ for J_y

Next, to calculate the divergence of flux a backward difference scheme is considered.

$$\begin{array}{c}
 J_y|_{i,j} \\
 \downarrow \\
 \bullet_{i,j+\frac{1}{2}} \\
 J_x|_{i-1,j} \quad \nabla \cdot J \quad J_x|_{i,j} \\
 \bullet_{i-\frac{1}{2},j} \quad \bullet_{i,j} \quad \bullet_{i+\frac{1}{2},j} \\
 \bullet_{i,j-\frac{1}{2}} \quad \qquad \qquad \qquad J_y|_{i,j-1}
 \end{array}$$

A.4 Voronoi tesselation for polycrystalline microstructure

A set of points $P = P_1, P_2, \dots, P_n$, named as node points, is taken randomly in an Euclidean plane. The number of points chosen is the same as the number of grains desired in the microstructure. Now, the Euclidean distance between all the other

points and the node points are measured. All those points which have the shortest distance from a given node points are part of that particular node point. In this way a polygonal domain is created around all the node points. Lines are generated between two adjacent domains, these are the grain boundaries. The points lying on these lines are equidistant from two adjacent node points. Assume, (a_1, b_1) is a node point and another point (c_1, d_1) in the Euclidean plane. The Euclidean distance between these two points is measured as

$$l_1 = \sqrt{(a_1 - c_1)^2 + (b_1 - d_1)^2} \quad (\text{A.1})$$

similarly, l_2, l_3, \dots, l_n is measured and the shortest of the l_i 's is taken out and the point (c_1, d_1) is assigned to the node point (a_i, b_i) .

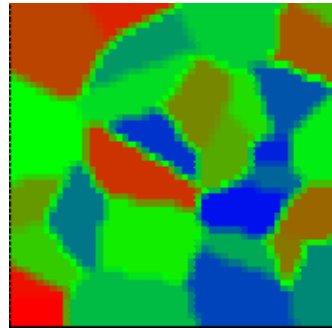


Figure A.9: Microstructure generated using Voronoi tessellation.

Bibliography

- [1] J. He, Z. Suo, Statistics of Electromigration Lifetime Analyzed Using a Deterministic Transient Model, AIP Conference Proceedings 12/2004; 741(1). DOI: 10.1063/1.1845832.
- [2] H. B. Huntington and A. R. Grone, Current-Induced Marker Motion in Gold Wires, *J. Phys. Chem. Solids*, vol. 20, no. 1, pp. 76-87, 1961.
- [3] W. W. Mullins, Theory of Thermal Grooving, *Journal of Applied Physics* 28, 333 (1957).
- [4] M. Ohring, Electromigration Damage in Thin Films due to Grain Boundary Grooving Processes, *Journal of Applied Physics* 42, 2653 (1971).
- [5] W. W. Mullins, The effect of thermal grooving on grain boundary motion, *Acta Metallurgica*, Volume 6, Issue 6, June 1958, Pages 414-427.
- [6] M. Mahadevan, R. M. Bradley, Phase field model of surface electromigration in single crystal metal thin films, *Physica D* 126 (1999) 201–213.
- [7] K. N. Tu, C. C. Yeh, C. Y. Liu, and Chih Chen, Effect of current crowding on vacancy diffusion and void formation in electromigration, *Appl. Phys. Lett.*, Vol. 76, No. 8, 21 February 2000.
- [8] D. N. Bhate, A. kumar, A. F. Bower, Diffuse interface model for electromigration and stress voiding, *J. Appl. Phys.* 87, 1712 (2000).
- [9] Abhik Choudhury and Britta Nestler, Grand-potential formulation for multicomponent phase transformations combined with thin-interface asymptotics of the double-obstacle potential, *Phys. Rev. E*, 10.1103/PhysRevE.85.021602.
- [10] N. Somaiah, D. Sharma, P. kumar, Electric current induced forward and anomalous backward mass transport, *J. Phys. D: Applied Physics*. 49(2016).

- [11] R. R. Mohanty, J. E. Guyer, Y. H. Sohn, Diffusion under temperature gradient: A phase-field model study, *JOURNAL OF APPLIED PHYSICS* 106, 034912 (2009).
- [12] L. Zhang, M. R. tonks, P. C. Millet, Y. Zhang, K. Chockalingam, B. Biner, Phase-field modeling of temperature gradient driven pore migration coupling with thermal conduction, *Computational Materials Science* 56 (2012) 161–165.
- [13] B. Nestler, F. Wendler, and M. Selzer, Phase-field model for multiphase systems with preserved volume fractions, *Phys. Rev. E* 78, 011604 (2008).
- [14] B. Nestler, H. Garcke, B. Stinner, Multicomponent alloy solidification: Phase-field modeling and simulations, *Phys. Rev. E* 71, 041609 (2005).
- [15] S. Shingubara, H. Kaneko, M. Saitoh, Electromigration induced abrupt changes in electrical resistance associated with void dynamics in aluminum interconnections, *J. Appl. Phys.* 69, 207 (1991).
- [16] Weiqing Wang and Z. Suo, A simulation of electromigration-induced transgranular slits, *J. Appl. Phys.* 79, 2394 (1996); <http://dx.doi.org/10.1063/1.361166>.
- [17] F. Y. Genin, W. W. Mullins, P. Wynblatt, Capillary instabilities in thin films: A model of thermal at grain boundary vertices. *Acta Metall. Mater.* 40(12):3239-3248, 1992.
- [18] D. J. Srolovitz and S. A. Safran, Capillary instabilities in thin films. I. Energetics, *Journal of Applied Physics* 60 ,247 (1986).
- [19] R. Rosenberg and M. Ohring, Void Formation and Growth During Electromigration in Thin Films, *Journal of Applied Physics* 42 , 5671 (1971).
- [20] F.Y. Genin, Surface Morphological Evolution of Thin Films Under Stress and Capillary Forces, *Interface science*, April 2001, Volume 9, Issue 1, pp 83-92.